

1 High-level cognition during story listening is reflected in
2 high-order dynamic correlations in neural activity patterns

3 Lucy L. W. Owen¹, Thomas H. Chang^{1,2}, and Jeremy R. Manning^{1,†}

¹Department of Psychological and Brain Sciences,
Dartmouth College, Hanover, NH

²Amazon.com, Seattle, WA

†Address correspondence to jeremy.r.manning@dartmouth.edu

4 November 20, 2020

5 **Abstract**

6 Our thoughts arise from coordinated patterns of interactions between brain structures that change with
7 our ongoing experiences. High-order dynamic correlations in neural activity patterns reflect different sub-
8 graphs of the brain's functional connectome that display homologous lower-level dynamic correlations. We
9 tested the hypothesis that high-level cognition is supported by reflected in high-order dynamic correlations
10 in brain activity patterns. We developed an approach to estimating high-order dynamic correlations in
11 timeseries data, and we applied the approach to neuroimaging data collected as human participants either
12 listened to a ten-minute story or listened to a temporally scrambled version of the story, or underwent
13 a resting-state scan. We trained across-participant pattern classifiers to decode (in held-out data) when in
14 the session each neural activity snapshot was collected. We found that classifiers trained to decode from
15 high-order dynamic correlations yielded the best performance on data collected as participants listened
16 to the (unscrambled) story. By contrast, classifiers trained to decode data from scrambled versions of the
17 story or during the resting state scan yielded the best performance when they were trained using first-
18 order dynamic correlations or non-correlational activity patterns. We suggest that as our thoughts become
19 more complex, they are supported by reflected in higher-order patterns of dynamic network interactions
20 throughout the brain.

21 **Introduction**

22 A central goal in cognitive neuroscience is to elucidate the *neural code*: the mapping between (a) mental
23 states or cognitive representations and (b) neural activity patterns. One means of testing models of the
24 neural code is to ask how accurately that model is able to "translate" neural activity patterns into known
25 (or hypothesized) mental states or cognitive representations (e.g., Haxby et al., 2001; Huth et al., 2016, 2012;
26 Kamitani & Tong, 2005; Mitchell et al., 2008; Nishimoto et al., 2011; Norman et al., 2006; Pereira et al.,
27 2018; Tong & Pratte, 2012). Training decoding models on different types of neural features (Fig. 1a) can
28 also help to elucidate which specific aspects of neural activity patterns are informative about cognition—
29 and, by extension, which types of neural activity patterns might comprise compose the neural code. For
30 example, prior work has used region of interest analyses to estimate the anatomical locations of specific

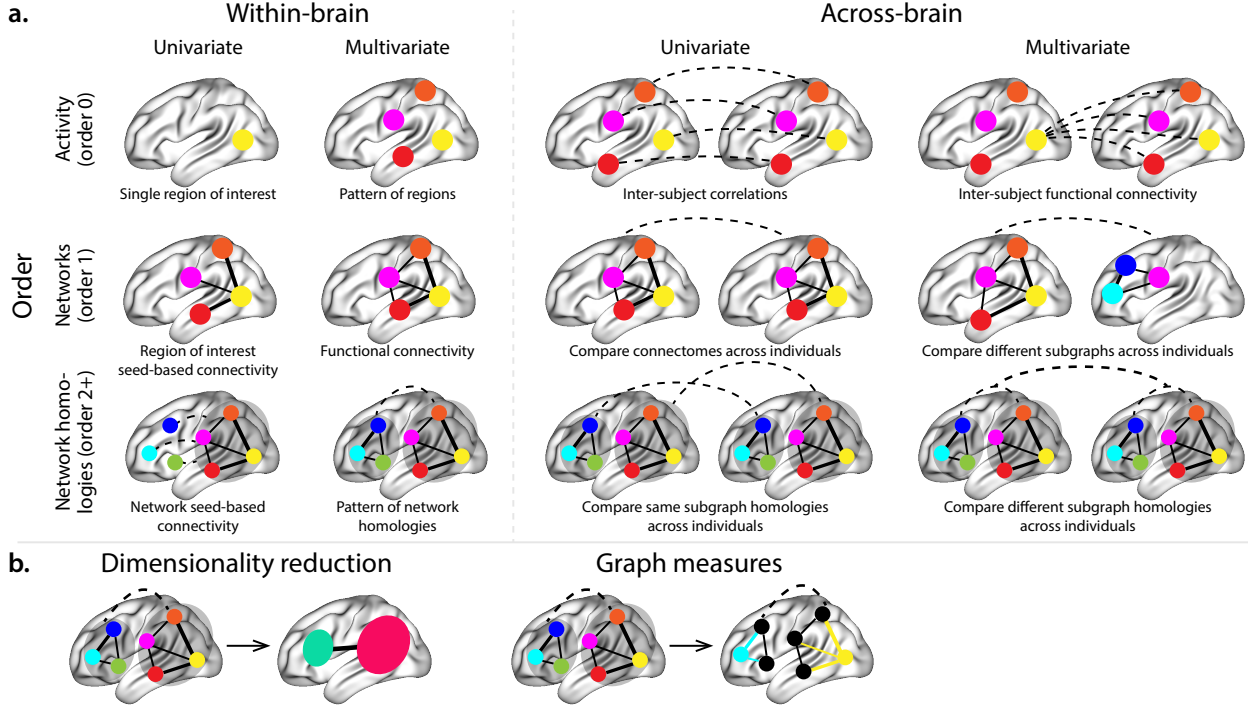


Figure 1: Neural patterns. a. A space of neural features. Within-brain analyses are carried out within a single brain, whereas across-brain analyses compare neural patterns across two or more individuals' brains. Univariate analyses characterize the activities of individual units (e.g., nodes, small networks, hierarchies of networks, etc.), whereas multivariate analyses characterize the patterns of activities across units. Order 0 patterns involve individual nodes; order 1 patterns involve node-node interactions; order 2 (and higher) patterns relate to interactions between homologous networks. Each of these patterns may be static (e.g., averaging over time) or dynamic. **b. Summarizing neural patterns.** To efficiently compute with complex neural patterns, it can be useful to characterize the patterns using summary measures. Dimensionality reduction algorithms project the patterns onto lower-dimensional spaces whose dimensions reflect weighted combinations or non-linear transformations of the dimensions in the original space. Graph measures characterize each unit's participation in its associated network.

31 neural representations (e.g., Etzel et al., 2009), or to compare the relative contributions to the neural code of
 32 multivariate activity patterns versus dynamic correlations between neural activity patterns (e.g., Fong et al.,
 33 2019; Manning et al., 2018). An emerging theme in this literature is that cognition is mediated by dynamic
 34 interactions between brain structures (Bassett et al., 2006; Demertzi et al., 2019; Friston, 2000; Grossberg,
 35 1988; Lurie et al., 2018; Mack et al., 2017; Preti et al., 2017; Solomon et al., 2019; Sporns & Honey, 2006;
 36 Turk-Browne, 2013; Zou et al., 2019).

37 Studies of the neural code to date have primarily focused on univariate or multivariate neural pat-
 38 terns (for review see Norman et al., 2006), or (more recently) on patterns of dynamic first-order corre-
 39 lations (i.e., interactions between pairs of brain structures; Demertzi et al., 2019; Fong et al., 2019; Lurie et al.,
 40 2018; Manning et al., 2018; Preti et al., 2017; Zou et al., 2019). **We wondered what What might** the future

41 of this line of work ~~might hold~~. hold? For example, is the neural code ~~mediated by~~ implemented through
42 higher-order interactions between brain structures (e.g., see Reimann et al., 2017)? Second-order correlations
43 reflect *homologous* patterns of correlation. In other words, if the dynamic patterns of correlations between
44 two regions, *A* and *B*, are similar to those between two other regions, *C* and *D*, this would be reflected
45 in the second-order correlations between (*A*-*B*) and (*C*-*D*). In this way, second-order correlations identify
46 similarities and differences between subgraphs of the brain’s connectome. Analogously, third-order cor-
47 relations reflect homologies between second-order correlations—i.e., homologous patterns of homologous
48 interactions between brain regions. More generally, higher-order correlations reflect homologies between
49 patterns of lower-order correlations. We can then ask: which “orders” of interaction are most reflective of
50 high-level cognitive processes?

51 One reason one might expect to see homologous networks in a dataset is related to the notion that
52 network dynamics reflect ongoing neural computations or cognitive processing (e.g., Beatty et al., 2016). If
53 the nodes in two brain networks are interacting (within each network) in similar ways then, according to
54 our characterization of network dynamics, we refer to the similarities between those patterns of interaction
55 as higher-order correlations. When higher-order correlations are themselves changing over time, we can
56 also attempt to capture and characterize those high-order dynamics.

57 Another central question pertains to the extent to which the neural code is carried by activity patterns
58 that directly reflect ongoing cognition (e.g., following Haxby et al., 2001; Norman et al., 2006), versus the
59 dynamic properties of the network structure itself, independent of specific activity patterns in any given
60 set of regions (e.g., following Bassett et al., 2006). For example, graph measures such as centrality and
61 degree (Bullmore & Sporns, 2009) may be used to estimate how a given brain structure is “communicating”
62 with other structures, independently of the specific neural representations carried by those structures.
63 If one considers a brain region’s position in the network (e.g., its eigenvector centrality) as a dynamic
64 property, one can compare how the positions of different regions are correlated, and/or how those patterns
65 of correlations change over time. We can also compute higher-order patterns in these correlations to
66 characterize homologous subgraphs in the connectome that display similar changes in their constituent
67 brain structures’ interactions with the rest of the brain.

68 To gain insights into the above aspects of the neural code, we developed a computational framework
69 for estimating dynamic high-order correlations in timeseries data. This framework provides an important
70 advance, in that it enables us to examine patterns of higher-order correlations that are computationally
71 intractable to estimate via conventional methods. Given a multivariate timeseries, our framework provides
72 timepoint-by-timepoint estimates of the first-order correlations, second-order correlations, and so on. Our
73 approach combines a kernel-based method for computing dynamic correlations in timeseries data with a di-

74 dimensionality reduction step (Fig. 1b) that projects the resulting dynamic correlations into a low-dimensional
75 space. We explored two dimensionality reduction approaches: principle components analysis (PCA; Pear-
76 son, 1901), which preserves an approximately invertible transformation back to the original data (e.g., this
77 follows related approaches taken by Gonzalez-Castillo et al., 2019; McIntosh & Jirsa, 2019; Toker & Som-
78 mer, 2019); and a second non-invertible algorithm that explored patterns in eigenvector centrality (Landau,
79 1895). This latter approach characterizes correlations between each feature dimension's relative *position* in
80 the network in favor of the specific activity histories of different features (also see Betzel et al., 2019; Reimann
81 et al., 2017; Sizemore et al., 2018).

82 We validated our approach using synthetic data where the underlying correlations were known. We then
83 applied our framework to a neuroimaging dataset collected as participants listened to either an audio record-
84 ing of a ten-minute story, listened to a temporally scrambled version of the story, or underwent a resting state
85 scan (Simony et al., 2016). Temporal scrambling has been used in a growing number of studies, largely by Uri
86 Hasson's group, to identify brain regions that are sensitive to higher-order and longer-timescale information
87 (e.g., cross-sensory integration, rich narrative meaning, complex situations, etc.) versus regions that are
88 primarily sensitive to low-order (e.g., sensory) information. For example, Hasson et al. (2008) argues that
89 when brain areas are sensitive to fine versus coarse temporal scrambling, this indicates that they are "higher
90 order" in the sense that they process contextual information pertaining to further-away timescales. By
91 contrast, low-level regions, such as primary sensory cortices, do not meaningfully change their responses
92 (after correcting for presentation order) even when the stimulus is scrambled at fine timescales.

93 We used a subset of the story listening and rest data to train across-participant classifiers to decode
94 listening times (of groups of participants) using a blend of neural features (comprising neural activity
95 patterns, as well as different orders of dynamic correlations between those patterns that were inferred
96 using our computational framework). We found that both the PCA-based and eigenvector centrality-based
97 approaches yielded neural patterns that could be used to decode accurately (i.e., well above chance). Both
98 approaches also yielded the best decoding accuracy for data collected during (intact) story listening when
99 high-order (PCA: second-order; eigenvector centrality: fourth-order) dynamic correlation patterns were
100 included as features. When we trained classifiers on the scrambled stories or resting state data, only
101 (relatively) lower-order dynamic patterns were informative to the decoders. Taken together, our results
102 indicate that high-level cognition is supported by high-order dynamic patterns of communication between
103 brain structures.

104 **Results**

105 We sought to understand whether high-level cognition is ~~supported by reflected in~~ dynamic patterns of high-
106 order correlations. To that end, we developed a computational framework for estimating the dynamics of
107 stimulus-driven high-order correlations in multivariate timeseries data (see *Dynamic inter-subject functional*
108 *connectivity (DISFC)* and *Dynamic higher-order correlations*). We evaluated the efficacy of this framework at
109 recovering known patterns in several synthetic datasets (see *Synthetic data: simulating dynamic first-order*
110 *correlations and Synthetic data: simulating dynamic higher-order correlations*). We then applied the framework
111 to a public fMRI dataset collected as participants listened to an ~~auditorily~~ auditorily presented story,
112 listened to a temporally scrambled version of the story, or underwent a resting state scan (see *Functional*
113 *neuroimaging data collected during story listening*). We used the relative decoding accuracies of classifiers
114 trained on different sets of neural features to estimate which types of features reflected ongoing cognitive
115 processing.

116 **Recovering known dynamic correlations from synthetic data**

117 **Recovering dynamic first-order correlations**

118 We generated synthetic datasets that differed in how the underlying first-order correlations changed over
119 time. For each dataset, we applied Equation 4 with a variety of kernel shapes and widths. We assessed how
120 well the true underlying correlations at each timepoint matched the recovered correlations (Fig. 2). For every
121 kernel and dataset we tested, our approach recovered the correlation dynamics we embedded into the data.
122 However, the quality of these recoveries varied across different synthetic datasets in a kernel-dependent
123 way.

124 In general, wide monotonic kernel shapes (Laplace, Gaussian), and wider kernels (within a shape),
125 performed best when the correlations varied gradually from moment-to-moment (Figs. 2a, c, and d). In the
126 extreme, as the rate of change in correlations approaches 0 (Fig. 2a), an infinitely wide kernel would exactly
127 recover the Pearson's correlation (e.g., compare Eqns. 1 and 4).

128 When the correlation dynamics were unstructured in time (Fig. 2b), a Dirac δ kernel (infinitely narrow)
129 performed best. This is because, when every timepoint's correlations are independent of the correlations at
130 every other timepoint, averaging data over time dilutes the available signal. Following a similar pattern,
131 holding kernel shape fixed, narrower kernel parameters better recovered randomly varying correlations.

132 **Recovering dynamic higher-order correlations**

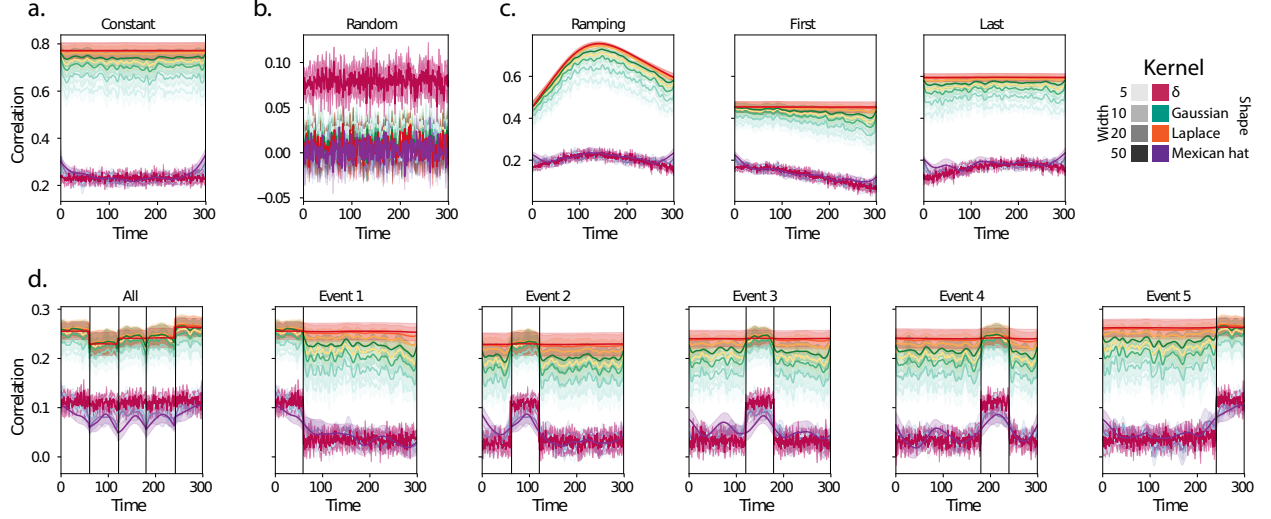


Figure 2: **Recovering known dynamic correlations from synthetic data.** **Recovering known dynamic first-order correlations from synthetic data.** Each panel displays the average correlations between the vectorized upper triangles of the recovered correlation matrix at each timepoint and either the true underlying correlation at each timepoint or a reference correlation matrix. (The averages are taken across 10 different randomly generated synthetic datasets of the given category.) Error ribbons denote 95% confidence intervals (taken across datasets). Different colors denote different kernel shapes, and the shading within each color family denotes the kernel width parameter. For a complete description of each synthetic dataset, see [Synthetic data](#)
Synthetic data: simulating dynamic first-order correlations. **a. Constant correlations.** These datasets have a stable (unchanging) underlying correlation matrix. **b. Random correlations.** These datasets are generated using a new independently drawn correlation matrix at each new timepoint. **c. Ramping correlations.** These datasets are generated by smoothly varying the underlying correlations between the randomly drawn correlation matrices at the first and last timepoints. The left panel displays the correlations between the recovered dynamic correlations and the underlying ground truth correlations. The middle panel compares the recovered correlations with the *first* timepoint’s correlation matrix. The right panel compares the recovered correlations with the *last* timepoint’s correlation matrix. **d. Event-based correlations.** These datasets are each generated using five randomly drawn correlation matrices that each remain stable for a fifth of the total timecourse. The left panel displays the correlations between the recovered dynamic correlations and the underlying ground truth correlations. The right panels compare the recovered correlations with the correlation matrices unique to each event. The vertical lines denote event boundaries.

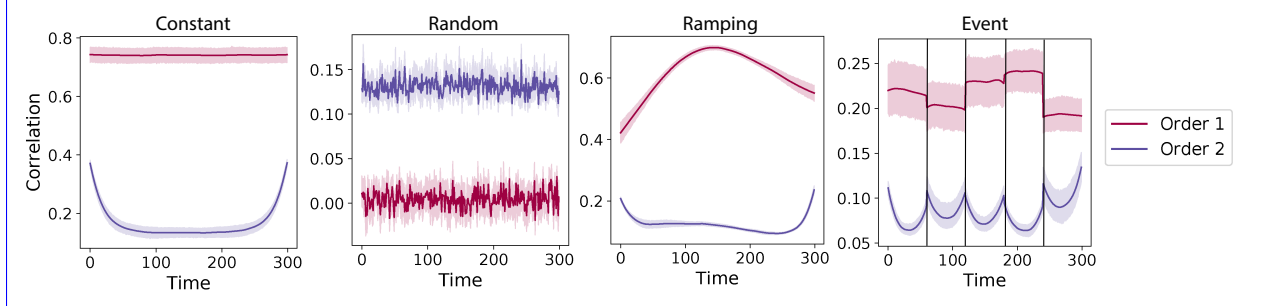


Figure 3: **Recovery of simulated first-order and second-order dynamic correlations.** Each panel displays the average correlations between the vectorized upper triangles of the recovered first-order and second-order correlation matrices and the true (simulated) first-order and second order correlation matrices at each timestep and for each synthetic dataset. (The averages are taken across 10 different randomly generated synthetic datasets of the given category.) Error ribbons denote 95% confidence intervals (taken across datasets). For a complete description of each synthetic dataset, see *Synthetic data: simulating dynamic higher-order correlations*. All estimates represented in this figure were computed using a Laplace kernel (width = 20). **a. Constant correlations.** These datasets have stable (unchanging) underlying second-order correlation matrices. **b. Random correlations.** These datasets are generated using a new independently drawn second-order correlation matrix at each timestep. **c. Ramping correlations.** These datasets are generated by smoothly varying the underlying second-order correlations between the randomly drawn correlation matrices at the first and last timepoints. **d. Event-based correlations.** These datasets are each generated using five randomly drawn second-order correlation matrices that each remain stable for a fifth of the total timecourse. The vertical lines denote event boundaries.

Following our approach to evaluating our ability to recover known dynamic first-order correlations from synthetic data, we generated an analogous second set of synthetic datasets that we designed to exhibit known dynamic first-order and second-order correlations (see *Synthetic data: simulating dynamic higher-order correlations*). We generated a total of 40 datasets that varied in how the first-order and second-order correlations changed over time. We then repeatedly applied Equation 4 using the overall best-performing kernel from our first-order tests (a Laplace kernel with a width of 20; Fig. 2) to assess how closely the recovered dynamic correlations matched the dynamic correlations we had embedded into the datasets.

Overall, we found that we could reliably recover both first-order and second-order correlations from the synthetic data (Fig. 3). When the correlations were stable for longer intervals, or changed gradually (constant, ramping, and event datasets), recovery performance was relatively high, and we were better able to recover dynamic first-order correlations than second-order correlations. We expected that this would happen, given that errors in our estimation procedure at lower orders necessarily propagate to higher orders (since lower-order correlations are used to estimate higher-order correlations). Interestingly, we also found that when the correlations were particularly unstable (random datasets), we better recovered second-order correlations.

Taken together, our explorations using synthetic data indicated that we are able to partially, but not perfectly, recover ground truth dynamic first-order and second-order correlations. This suggests that our

150 modeling approach provides a meaningful (if noisy) estimate of high-order correlations. We next turned
151 to analyses of human fMRI data to examine whether the recovered dynamics might reflect the dynamics of
152 human cognition during a naturalistic story-listening task.

153 Cognitively relevant dynamic high-order correlations in fMRI data

154 We used across-participant temporal decoders to identify cognitively relevant neural patterns in fMRI data
155 (see *Forward inference and decoding accuracy*). The dataset we examined (collected by Simony et al., 2016)
156 comprised four experimental conditions that exposed participants to stimuli that varied systematically in
157 how cognitively engaging they were. The *intact* experimental condition had participants listen to an audio
158 recording of a 10-minute story. The *paragraph*-scrambled experimental condition had participants listen to a
159 temporally scrambled version of the story, where the paragraphs occurred out of order (but where the same
160 total set of paragraphs were presented over the full listening interval). All participants in this condition
161 experienced the scrambled paragraphs in the same order. The *word*-scrambled experimental condition had
162 participants listen to a temporally scrambled version of the story where the words in the story occurred
163 in a random order. All participants in the word condition experienced the scrambled words in the same
164 order. Finally, in a *rest* experimental condition, participants lay in the scanner with no overt stimulus, with
165 their eyes open (blinking as needed). This dataset provided a convenient means of testing our hypothesis
166 that different levels of cognitive processing and engagement are supported by reflected in different orders
167 of brain activity dynamics.

168 In brief, we computed timeseries of dynamic high-order correlations that were similar across participants
169 in each of two randomly assigned groups: a training group and a test group. We then trained classifiers
170 on the training group's data to match each sample from the test group with a stimulus timepoint. Each
171 classifier comprised a weighted blend of neural patterns that reflected up to n^{th} -order dynamic correlations
172 (see *Feature weighting and testing*, Fig. 10). We repeated this process for $n \in \{0, 1, 2, \dots, 10\}$. Our examinations
173 of synthetic data suggested that none of the kernels we examined were "universal" in the sense of optimally
174 recovering underlying correlations regardless of the temporal structure of those correlations. We found a
175 similar pattern in the (real) fMRI data, whereby different kernels yielded different decoding accuracies, but
176 no single kernel emerged as the clear "best." In our analyses of neural data, we therefore averaged our
177 decoding results over a variety of kernel shapes and widths in order to identify results that were robust to
178 specific kernel parameters (see *Identifying robust decoding results*).

179 Our approach to estimating dynamic high-order correlations entails mapping the high-dimensional
180 feature space of correlations (represented by a T by $O(K^2)$ matrix) onto a lower-dimensional feature space

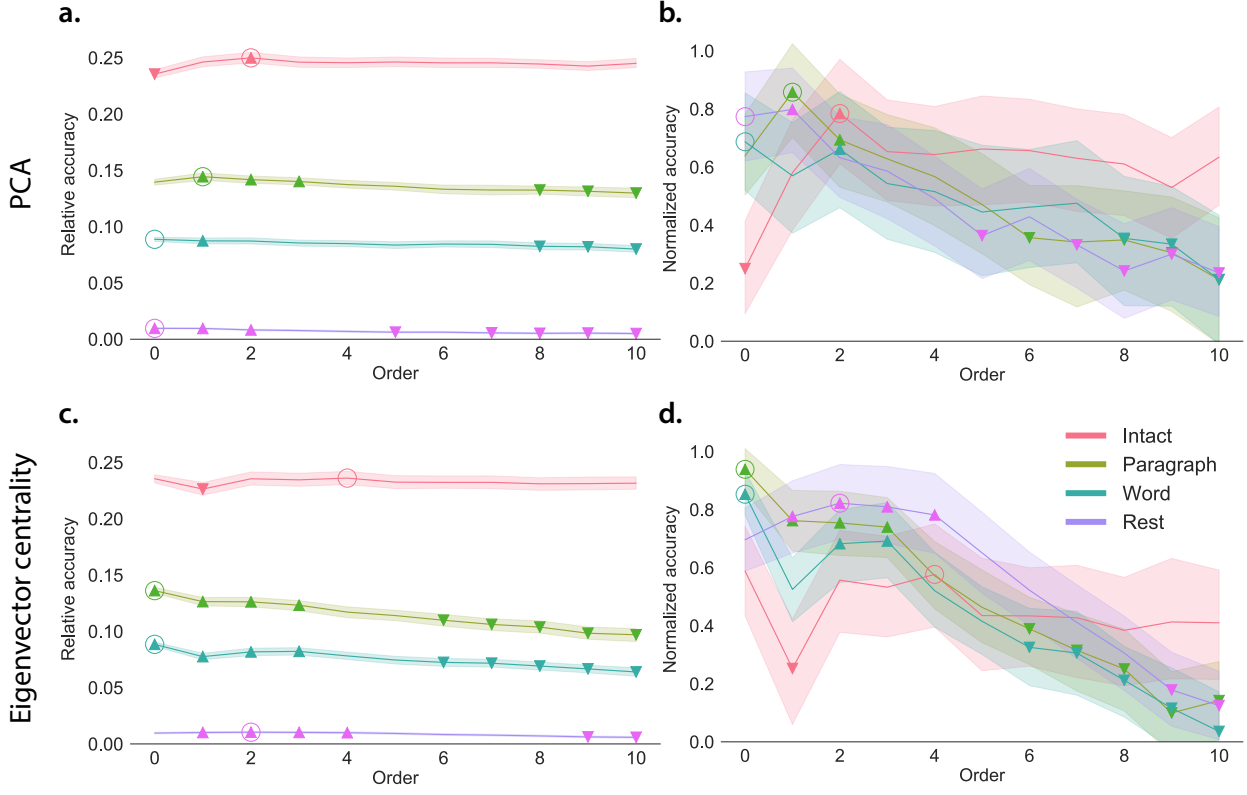


Figure 4: **Across-participant decoding accuracy varies with correlation order and cognitive engagement.** **Across-participant timepoint decoding accuracy varies with correlation order and cognitive engagement.**

a. Decoding accuracy as a function of order: PCA. Order (x-axis) refers to the maximum order of dynamic correlations that were available to the classifiers (see *Feature weighting and testing*). The reported across-participant decoding accuracies are averaged over all kernel shapes and widths (see *Identifying robust decoding results*). The y-values are displayed relative to chance accuracy (intact: $\frac{1}{300}$; paragraph: $\frac{1}{272}$; word: $\frac{1}{300}$; rest: $\frac{1}{400}$). The error ribbons denote 95% confidence intervals across cross-validation folds (i.e., random assignments of participants to the training and test sets). The colors denote the experimental condition. Arrows denote sets of features that yielded reliably higher (upwards facing) or lower (downward facing) decoding accuracy than the mean of all other features (via a two-tailed test, thresholded at $p < 0.05$). Figure 5 displays additional comparisons between the decoding accuracies achieved using different sets of neural features. The circled values represent the maximum decoding accuracy within each experimental condition.

b. Normalized decoding accuracy as a function of order: PCA. This panel displays the same results as Panel a, but here each curve has been normalized to have a maximum value of 1 and a minimum value of 0 (including the upper and lower bounds of the respective 95% confidence intervals). Panels a and b used PCA to project each high-dimensional pattern of dynamic correlations onto a lower-dimensional space.

c. Decoding accuracy as a function of order: eigenvector centrality.

d. Normalized decoding accuracy as a function of order: eigenvector centrality.

e. Decoding accuracy as a function of order: eigenvector centrality.

f. Normalized timepoint decoding accuracy as a function of order: eigenvector centrality.

This panel is in the same format as Panel a, but here eigenvector centrality has been used to project the high-dimensional patterns of dynamic correlations onto a lower-dimensional space.

g. Normalized timepoint decoding accuracy as a function of order: eigenvector centrality.

This panel is in the same format as Panel b, but here eigenvector centrality has been used to project the high-dimensional patterns of dynamic correlations onto a lower-dimensional space.

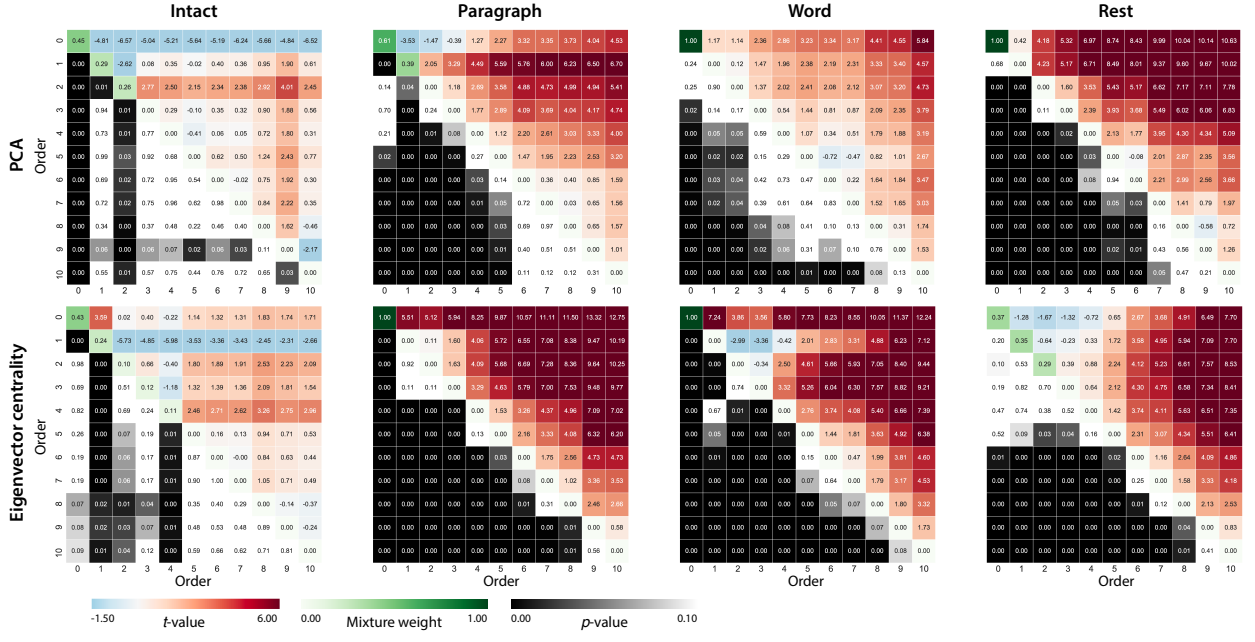


Figure 5: Statistical summary of decoding accuracies for different neural features. Each column of matrices displays decoding results for one experimental condition (intact, paragraph, word, and rest). We considered dynamic activity patterns (order 0) and dynamic correlations at different orders (order > 0). We used two-tailed t -tests to compare the distributions of decoding accuracies obtained using each pair of features. The distributions for each feature reflect the set of average decoding accuracies (across all kernel parameters), obtained for each random assignment of training and test groups. In the upper triangles of each map, warmer colors (positive t -values) indicate that the neural feature indicated in the given row yielded higher accuracy than the feature indicated in the given column. Cooler colors (negative t -values) indicate that the feature in the given row yielded lower decoding accuracy than the feature in the given column. The lower triangles of each map denote the corresponding p -values for the t -tests. The diagonal entries display the relative average optimized weight given to each type of feature, in a decoder that included all feature types (see *Feature weighting and testing*).

181 (represented by a T by K matrix). We carried out two sets of analyses that differed in how this mapping was
 182 computed. The first set of analyses used PCA to find a low-dimensional embedding of the original dynamic
 183 correlation matrices (Fig. 4a,b). The second set of analyses characterized correlations in dynamics of each
 184 feature's eigenvector centrality, but did not preserve the underlying activity dynamics (Fig. 4c,d).

185 Both sets of temporal decoding analyses yielded qualitatively similar results for the auditory (non-rest)
 186 conditions of the experiment (Fig. 4: pink, green, and teal lines; Fig. 5: three leftmost columns). The highest
 187 decoding accuracy for participants who listened to the intact (unscrambled) story was achieved using high-
 188 order dynamic correlations (PCA: second-order; eigenvector-centrality: fourth-order). Scrambled versions
 189 of the story were best decoded by lower-order correlations (PCA/paragraph: first-order; PCA/word: order
 190 zero; eigenvector centrality/paragraph: order zero; eigenvector centrality/word: order zero). The two sets
 191 of analyses yielded different decoding results on resting state data (Fig. 4: purple lines; Fig. 5: rightmost
 192 column). We note that while the resting state times could be decoded reliably, the accuracies were only very

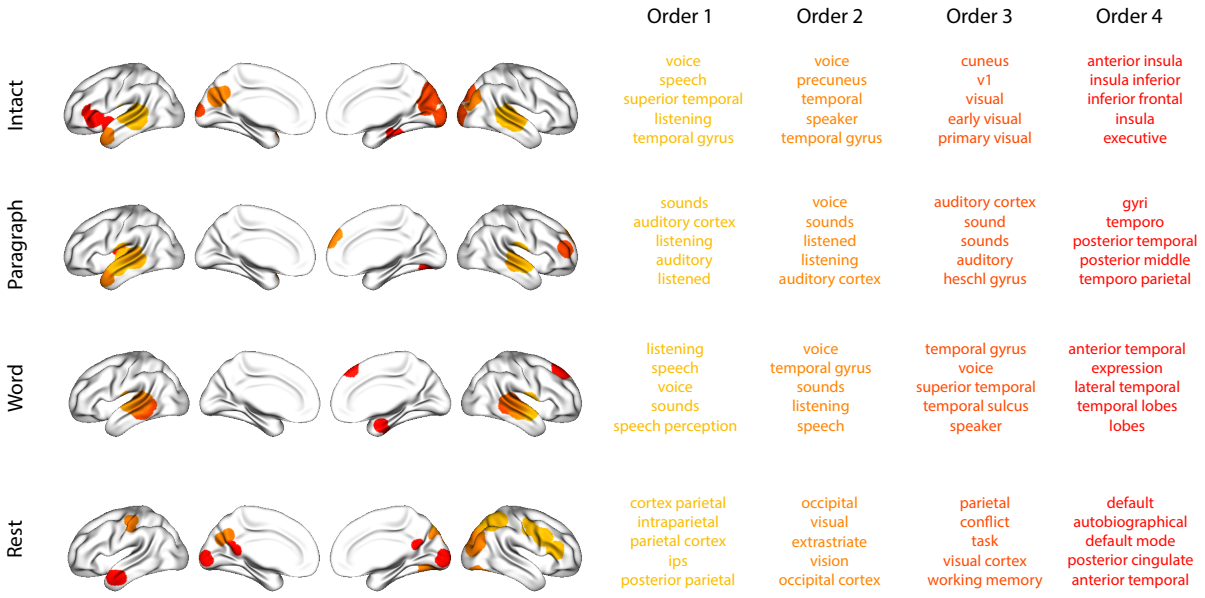


Figure 6: Top terms associated with the endpoints of the strongest correlations. Each color corresponds to one order of inter-subject functional correlations. To calculate the dynamic correlations, eigenvector centrality has been used to project the high-dimensional patterns of dynamic correlations onto a lower-dimensional space at each previous order, which allows us the map the brain regions at each order by retaining the features of the original space. The inflated brain plots display the locations of the endpoints of the 10 strongest (absolute value) correlations at each order, thresholded at 0.999, and projected onto the cortical surface (Combrisson et al., 2019). The lists of terms on the right display the top five Neurosynth terms (Rubin et al., 2017) decoded from the corresponding brain maps for each order. Each row displays data from a different experimental condition. Additional maps and their corresponding Neurosynth terms may be found in the *Supplementary materials* (intact: Fig. S1; paragraph: Fig. S2; word: Fig. S3; rest: Fig. S4).

193 slightly above chance. We speculate that the decoders might have picked up on attentional drift, boredom,
 194 or tiredness; we hypothesize that these all increased throughout the resting state scan. The decoders might
 195 be picking up on aspects of these loosely defined cognitive states that are common across individuals. The
 196 PCA-based approach achieved the highest resting state decoding accuracy using order zero features (non-
 197 correlational, activation-based), whereas the eigenvector centrality-based approach achieved the highest
 198 resting state decoding accuracy using second-order correlations. Taken together, these analyses indicate
 199 that high-level cognitive processing (while listening to the intact story) is reflected in the dynamics of high-
 200 order correlations in brain activity, whereas lower-level cognitive processing (while listening to scrambled
 201 versions of the story that lack rich meaning) is reflected in the dynamics of lower-order correlations and
 202 non-correlational activity dynamics. Further, these patterns are associated both with the underlying activity
 203 patterns (characterized using PCA) and also with the changing relative positions that different brain areas
 204 occupy in their associated networks (characterized using eigenvector centrality).

205 Having established that patterns of high-order correlations are informative to decoders, we next won-

206 dered which specific networks of brain regions contributed most to these patterns. As a representative
207 example, we selected the kernel parameters that yielded decoding accuracies that best matched the average
208 accuracies across all of the kernel parameters we examined. Using Figure 4c as a template, the best-matching
209 kernel was a Laplace kernel with a width of 50 (Fig. 9d). We used this kernel to compute a single K by K
210 n^{th} -order DISFC matrix for each experimental condition. We then used Neurosynth (Rubin et al., 2017) to
211 compute the terms most highly associated with the most strongly correlated pairs of regions in each of these
212 matrices (Fig. 6; see *Reverse inference*).

213 For all of the story listening conditions (intact, paragraph, and word), we found that first- and second-
214 order correlations were most strongly associated with auditory and speech processing areas. During
215 intact story listening, third-order correlations reflected integration with visual areas, and fourth-order
216 correlations reflected integration with areas associated with high-level cognition and cognitive control,
217 such as the ventrolateral prefrontal cortex. However, during listening to temporally scrambled stories,
218 these higher-order correlations instead involved interactions with additional regions associated with speech
219 and semantic processing. By contrast, we found a much different set of patterns in the resting state data.
220 First-order resting state correlations were most strongly associated with regions involved in counting and
221 numerical understanding. Second-order resting state correlations were strongest in visual areas; third-order
222 correlations were strongest in task-positive areas; and fourth-order correlations were strongest in regions
223 associated with autobiographical and episodic memory. We carried out analogous analyses to create maps
224 (and decode the top associated Neurosynth terms) for up to fifteenth-order correlations (Figs. S1, S2, S3, and
225 S4). Of note, examining fifteenth-order correlations between 700 nodes using conventional methods would
226 have required storing roughly $\frac{700^{2 \times 15}}{2} \approx 1.13 \times 10^{85}$ floating point numbers—assuming single-precision (32
227 bits each), this would require roughly 32 times as many bits as there are molecules in the known universe!
228 Although these fifteenth-order correlations do appear (visually) to have some well-formed structure, we
229 provide this latter example primarily as a demonstration of the efficiency and scalability of our approach.

230 Discussion

231 We tested the hypothesis that high-level cognition is ~~supported by~~ reflected in high-order brain network
232 dynamics (e.g., see Reimann et al., 2017; Solomon et al., 2019). We examined high-order network dynamics
233 in functional neuroimaging data collected during a story listening experiment. When participants listened
234 to an auditory recording of the story, participants exhibited similar high-order brain network dynamics. By
235 contrast, when participants instead listened to temporally scrambled recordings of the story, only lower-
236 order brain network dynamics were similar across participants. Our results indicate that higher orders of

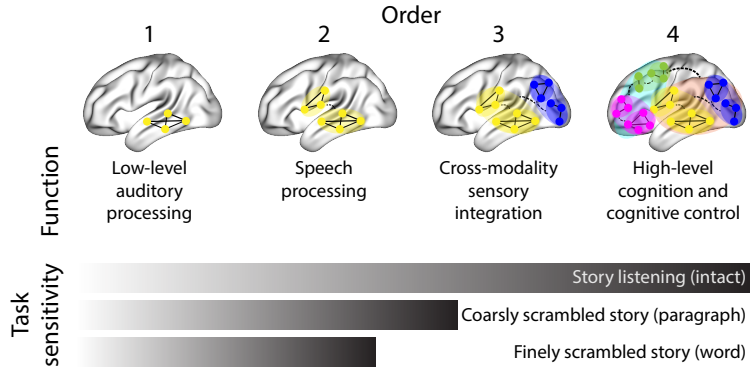


Figure 7: Proposed high-order network dynamics underlying high-level cognition during story listening. Higher Schematic depicts higher orders of network interactions support supporting higher-level aspects of cognitive processing. When tasks evoke richer, deeper, and/or higher-level processing, this is reflected in higher-order network interactions.

237 network interactions support higher-level aspects of cognitive processing (Fig. 7).

238 The notion that cognition is reflected in (and possibly mediated by) patterns of first-order network
 239 dynamics has been suggested by or proposed in myriad empirical studies and reviews (e.g., Chang &
 240 Glover, 2010; Demertzis et al., 2019; Fong et al., 2019; Gonzalez-Castillo et al., 2019; Liégeois et al., 2019; Lurie
 241 et al., 2018; Manning et al., 2018; Park et al., 2018; Preti et al., 2017; Roy et al., 2019; Turk-Browne, 2013;
 242 Zou et al., 2019). Our study extends this line of work by finding cognitively relevant *higher-order* network
 243 dynamics that reflect ongoing cognition. Our findings complement other work that uses graph theory and
 244 topology to characterize how brain networks reconfigure during cognition (e.g., Bassett et al., 2006; Betzel
 245 et al., 2019; McIntosh & Jirsa, 2019; Reimann et al., 2017; Sizemore et al., 2018; Toker & Sommer, 2019; Zheng
 246 et al., 2019).

247 An open question not addressed by our study pertains to how different structures integrate incom-
 248 ing information with different time constants. For example, one line of work suggests that the cortical
 249 surface comprises a structured map such that nearby brain structures process incoming information at
 250 similar timescales. Low-level sensory areas integrate information relatively quickly, whereas higher-level
 251 regions integrate information relatively slowly (Baldassano et al., 2017; Chien & Honey, 2019; Hasson et
 252 al., 2015, 2008; Honey et al., 2012; Lerner et al., 2014, 2011). A similar hierarchy appears to play a role in
 253 predicting future events (C. S. Lee et al., 2020). Other related work in human and mouse brains indicates
 254 that the temporal response profile of a given brain structure may relate to how strongly connected that
 255 structure is with other brain areas (Fallon et al., 2019). Further study is needed to understand the role of
 256 temporal integration at different scales of network interaction, and across different anatomical structures.
 257 Importantly, our analyses do not speak to the physiological basis of higher-order dynamics, and could reflect
 258 nonlinearities, chaotic patterns, non-stationarities, or multistability, etc. However, our decoding analyses

259 do indicate that higher-order dynamics are consistent across individuals, and therefore unlikely to be driven
260 by non-stimulus-driven dynamics which are unlikely to be similar across individuals.

261 Another potential limitation of our approach relates to recent work suggesting that the brain undergoes
262 rapid state changes, for example across event boundaries (e.g., Baldassano et al., 2017). Shappell et al.
263 (2019) used hidden semi-Markov models to estimate state-specific network dynamics (also see Vidaurre et
264 al., 2018). Our general approach might be extended by considering putative state transitions. For example,
265 rather than weighting all timepoints using a similar kernel (Eqn. 4), the kernel function could adapt on a
266 timepoint-by-timepoint basis such that only timepoints determined to be in the same “state” were given
267 non-zero weight.

268 Identifying high-order network dynamics associated with high-level cognition required several impor-
269 tant methods advances. First, we used kernel-based dynamic correlations to extended the notion of (static)
270 inter-subject functional connectivity (Simony et al., 2016) to a dynamic measure of inter-subject functional
271 connectivity (DISFC) that does not rely on sliding windows (e.g., as in Manning et al., 2018), and that may
272 be computed at individual timepoints. This allowed us to precisely characterize stimulus-evoked network
273 dynamics that were similar across individuals. Second, we developed a computational framework for
274 efficiently and scalably estimating high-order dynamic correlations. Our approach uses dimensionality
275 reduction algorithms and graph measures to obtain low-dimensional embeddings of patterns of network
276 dynamics. Third, we developed an analysis framework for identifying robust decoding results by carrying
277 out our analyses using a range of parameter values and then identifying which results were robust to specific
278 parameter choices.

279 Concluding remarks

280 The complex hierarchy of dynamic interactions that underlie our thoughts is perhaps the greatest mystery in
281 modern science. Methods for characterizing the dynamics of high-order correlations in neural data provide
282 a window into the neural basis of cognition. By showing that high-level cognition is reflected in high-order
283 network dynamics, we have elucidated the next step on the path towards understanding the neural basis
284 of cognition.

285 Methods

286 Our general approach to efficiently estimating high-order dynamic correlations comprises four general
287 steps (Fig. 8). First, we derive a kernel-based approach to computing dynamic pairwise correlations in

288 a T (timepoints) by K (features) multivariate timeseries, \mathbf{X}_0 . This yields a T by $O(K^2)$ matrix of dynamic
 289 correlations, \mathbf{Y}_1 , where each row comprises the upper triangle and diagonal of the correlation matrix at
 290 a single timepoint, reshaped into a row vector (this reshaped vector is $(\frac{K^2-K}{2} + K)$ -dimensional). Second,
 291 we apply a dimensionality reduction step to project the matrix of dynamic correlations back onto a K -
 292 dimensional space. This yields a T by K matrix, \mathbf{X}_1 , that reflects an approximation of the dynamic correlations
 293 reflected in the original data. Third, we use repeated applications of the kernel-based dynamic correlation
 294 step to \mathbf{X}_n and the dimensionality reduction step to the resulting \mathbf{Y}_{n+1} to estimate high-order dynamic
 295 correlations. Each application of these steps to a T by K time series \mathbf{X}_n yields a T by K matrix, \mathbf{X}_{n+1} , that
 296 reflects the dynamic correlations between the columns of \mathbf{X}_n . In this way, we refer to n as the *order* of the
 297 timeseries, where \mathbf{X}_0 (order 0) denotes the original data and \mathbf{X}_n denotes (approximated) n^{th} -order dynamic
 298 correlations between the columns of \mathbf{X}_0 . Finally, we use a cross-validation-based decoding approach to
 299 evaluate how well information contained in a given order (or weighted mixture of orders) may be used
 300 to decode relevant cognitive states. If including a given \mathbf{X}_n in the feature set yields higher classification
 301 accuracy on held-out data, we interpret this as evidence that the given cognitive states are reflected in
 302 patterns of n^{th} -order correlations.

303 All of the code used to produce the figures and results in this manuscript, along with links to the
 304 corresponding datasets, may be found at github.com/ContextLab/timecorr-paper. In addition, we have
 305 released a Python toolbox for computing dynamic high-order correlations in timeseries data; our toolbox
 306 may be found at timecorr.readthedocs.io.

307 Kernel-based approach for computing dynamic correlations

Given a T by K matrix of observations, \mathbf{X} , we can compute the (static) Pearson's correlation between any
 pair of columns, $\mathbf{X}(\cdot, i)$ and $\mathbf{X}(\cdot, j)$ using (Pearson, 1901):

$$\text{corr}(\mathbf{X}(\cdot, i), \mathbf{X}(\cdot, j)) = \frac{\sum_{t=1}^T (\mathbf{X}(t, i) - \bar{\mathbf{X}}(\cdot, i))(\mathbf{X}(t, j) - \bar{\mathbf{X}}(\cdot, j))}{\sqrt{\sum_{t=1}^T \sigma_{\mathbf{X}(\cdot, i)}^2 \sigma_{\mathbf{X}(\cdot, j)}^2}}, \text{ where} \quad (1)$$

$$\bar{\mathbf{X}}(\cdot, k) = \frac{1}{T} \sum_{t=1}^T \mathbf{X}(t, k), \text{ and} \quad (2)$$

$$\sigma_{\mathbf{X}(\cdot, k)}^2 = \frac{1}{T} \sum_{t=1}^T (\mathbf{X}(t, k) - \bar{\mathbf{X}}(\cdot, k))^2 \quad (3)$$

308 We can generalize this formula to compute time-varying correlations by incorporating a *kernel function* that
 309 takes a time t as input, and returns how much the observed data at each timepoint $\tau \in [-\infty, \infty]$ contributes
 310 to the estimated instantaneous correlation at time t (Fig. 9; also see Allen et al., 2012, for a similar approach).

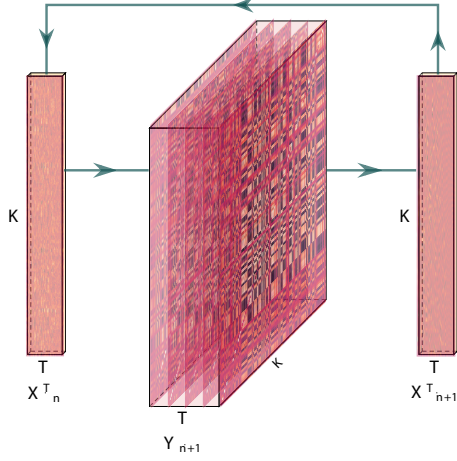


Figure 8: **Estimating dynamic high-order correlations.** Given a T by K matrix of multivariate timeseries data, \mathbf{X}_n (where $n \in \mathbb{N}, n \geq 0$), we use Equation 4 to compute a timeseries of K by K correlation matrices, \mathbf{Y}_{n+1} . We then approximate \mathbf{Y}_{n+1} with the T by K matrix \mathbf{X}_{n+1} . This process may be repeated to scalably estimate iteratively higher-order correlations in the data. Note that the transposes of \mathbf{X}_n and \mathbf{X}_{n+1} are displayed in the figure for compactness.

311

Given a kernel function $\kappa_t(\cdot)$ for timepoint t , evaluated at timepoints $\tau \in [1, \dots, T]$, we can update the static correlation formula in Equation 1 to estimate the *instantaneous correlation* at timepoint t :

$$\text{timecorr}_{\kappa_t}(\mathbf{X}(\cdot, i), \mathbf{X}(\cdot, j)) = \frac{\sum_{\tau=1}^T (\mathbf{X}(\tau, i) - \tilde{\mathbf{X}}_{\kappa_t}(\cdot, i))(\mathbf{X}(\tau, j) - \tilde{\mathbf{X}}_{\kappa_t}(\cdot, j))}{\sqrt{\sum_{\tau=1}^T \tilde{\sigma}_{\kappa_t}^2(\mathbf{X}(\cdot, i)) \tilde{\sigma}_{\kappa_t}^2(\mathbf{X}(\cdot, j))}}, \text{ where} \quad (4)$$

$$\tilde{\mathbf{X}}_{\kappa_t}(\cdot, k) = \sum_{\tau=1}^T \kappa_t(\tau) \mathbf{X}(\tau, k), \quad (5)$$

$$\tilde{\sigma}_{\kappa_t}^2(\mathbf{X}(\cdot, k)) = \sum_{\tau=1}^T (\mathbf{X}(\tau, k) - \tilde{\mathbf{X}}_{\kappa_t}(\cdot, k))^2. \quad (6)$$

312 Here $\text{timecorr}_{\kappa_t}(\mathbf{X}(\cdot, i), \mathbf{X}(\cdot, j))$ reflects the correlation at time t between columns i and j of \mathbf{X} , estimated using
 313 the kernel κ_t . We evaluate Equation 4 in turn for each pair of columns in \mathbf{X} and for kernels centered on each
 314 timepoint in the timeseries, respectively, to obtain a T by K by K timeseries of dynamic correlations, \mathbf{Y} . For
 315 convenience, we then reshape the upper triangles and diagonals of each timepoint's symmetric correlation
 316 matrix into a row vector to obtain an equivalent T by $(\frac{K^2-K}{2} + K)$ matrix.

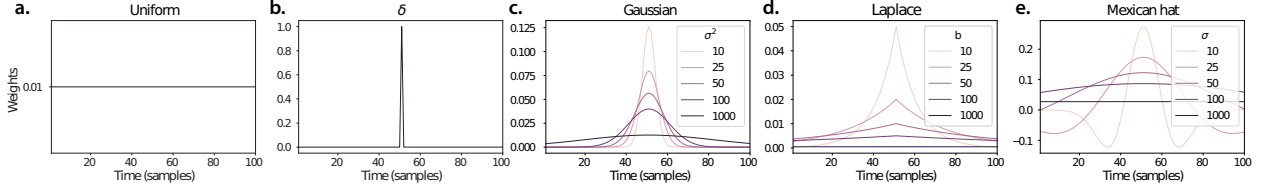


Figure 9: Examples of kernel functions. Each panel displays per-timepoint weights for a kernel centered at $t = 50$, evaluated at 100 timepoints ($\tau \in [1, \dots, 100]$). **a. Uniform kernel.** The weights are timepoint-invariant; observations at all timepoints are weighted equally, and do not change as a function of τ . This is a special case kernel function that reduces dynamic correlations to static correlations. **b. Dirac δ kernel.** Only the observation at timepoint t is given a non-zero weight (of 1). **c. Gaussian kernels.** Each kernel's weights fall off in time according to a Gaussian probability density function centered on time t . Weights derived using several different example width parameters (σ^2) are displayed. **d. Laplace kernels.** Each kernel's weights fall off in time according to a Laplace probability density function centered on time t . Weights derived using several different example width parameters (b) are displayed. **e. Mexican hat (Ricker wavelet) kernels.** Each kernel's weights fall off in time according to a Ricker wavelet centered on time t . This function highlights the *contrasts* between local versus surrounding activity patterns in estimating dynamic correlations. Weights derived using several different example width parameters (σ) are displayed.

317 Dynamic inter-subject functional connectivity (DISFC)

Equation 4 provides a means of taking a single observation matrix, \mathbf{X}_n and estimating the dynamic correlations from moment to moment, \mathbf{Y}_{n+1} . Suppose that one has access to a set of multiple observation matrices that reflect the same phenomenon. For example, one might collect neuroimaging data from several experimental participants, as each participant performs the same task (or sequence of tasks). Let $\mathbf{X}_n^1, \mathbf{X}_n^2, \dots, \mathbf{X}_n^P$ reflect the T by K observation matrices ($n = 0$) or reduced correlation matrices ($n > 0$) for each of P participants in an experiment. We can use *inter-subject functional connectivity* (ISFC; Simony & Chang, 2020; Simony et al., 2016) to compute the stimulus-driven correlations reflected in the multi-participant dataset at a given timepoint t using:

$$\bar{\mathbf{C}}(t) = M \left(R \left(\frac{1}{2P} \sum_{p=1}^P Z(\mathbf{Y}_{n+1}^p(t))^\top + Z(\mathbf{Y}_{n+1}^p(t)) \right) \right), \quad (7)$$

where M extracts and vectorizes the upper triangle and diagonal of a symmetric matrix, Z is the Fisher z-transformation (Zar, 2010):

$$Z(r) = \frac{\log(1+r) - \log(1-r)}{2}, \quad (8)$$

R is the inverse of Z :

$$R(z) = \frac{\exp(2z-1)}{\exp(2z+1)}, \quad (9)$$

and $\mathbf{Y}_{n+1}^p(t)$ denotes the correlation matrix at timepoint t (Eqn. 4) between each column of \mathbf{X}_n^p and each column of the average $\bar{\mathbf{X}}_n$ from all *other* participants, $\bar{\mathbf{X}}_n^{\setminus p}$:

$$\bar{\mathbf{X}}_n^{\setminus p} = \frac{1}{P-1} \sum_{q \in \setminus p} \mathbf{X}_n^q, \quad (10)$$

318 where $\setminus p$ denotes the set of all participants other than participant p . In this way, the T by $\left(\frac{K^2-K}{2} + K\right)$ DISFC
 319 matrix $\bar{\mathbf{C}}$ provides a time-varying extension of the ISFC approach developed by Simony et al. (2016).

320 Low-dimensional representations of dynamic correlations

321 Given a T by $\left(\frac{K^2-K}{2} + K\right)$ matrix of n^{th} -order dynamic correlations, \mathbf{Y}_n , we propose two general approaches
 322 to computing a T by K low-dimensional representation of those correlations, \mathbf{X}_n . The first approach uses
 323 dimensionality reduction algorithms to project \mathbf{Y}_n onto a K -dimensional space. The second approach uses
 324 graph measures to characterize the relative positions of each feature ($k \in [1, \dots, K]$) in the network defined
 325 by the correlation matrix at each timepoint.

326 Dimensionality reduction-based approaches to computing \mathbf{X}_n

327 The modern toolkit of dimensionality reduction algorithms include Principal Components Analysis (PCA;
 328 Pearson, 1901), Probabilistic PCA (PPCA; Tipping & Bishop, 1999), Exploratory Factor Analysis (EFA;
 329 Spearman, 1904), Independent Components Analysis (ICA; Comon et al., 1991; Jutten & Herault, 1991),
 330 t-Stochastic Neighbor Embedding (t-SNE; van der Maaten & Hinton, 2008), Uniform Manifold Approximation and Projection (UMAP; McInnes et al., 2018), non-negative matrix factorization (NMF; D. D. Lee
 331 & Seung, 1999), Topographic Factor Analysis (TFA; Manning et al., 2014), Hierarchical Topographic Factor analysis (HTFA; Manning et al., 2018), Topographic Latent Source Analysis (TLSA; Gershman et al.,
 332 2011), dictionary learning (J. Mairal et al., 2009; J. B. Mairal et al., 2009), and deep auto-encoders (Hinton
 333 & Salakhutdinov, 2006), among others. While complete characterizations of each of these algorithms is
 334 beyond the scope of the present manuscript, the general intuition driving these approaches is to compute
 335 the T by K matrix, \mathbf{X} , that is closest to the original T by J matrix, \mathbf{Y} , where (typically) $K \ll J$. The different
 336 approaches place different constraints on what properties \mathbf{X} must satisfy and which aspects of the data are
 337 compared (and how) in order to optimize how well \mathbf{X} approximates \mathbf{Y} .

338 Applying dimensionality reduction algorithms to \mathbf{Y} yields an \mathbf{X} whose columns reflect weighted combinations (or nonlinear transformations) of the original columns of \mathbf{Y} . This has two main consequences.
 339 First, with each repeated dimensionality reduction, the resulting \mathbf{X}_n has lower and lower fidelity (with

respect to what the “true” \mathbf{Y}_n might have looked like without using dimensionality reduction to maintain ~~scalability~~tractability). In other words, computing \mathbf{X}_n is a lossy operation. Second, whereas each column of \mathbf{Y}_n may be mapped directly onto specific pairs of columns of \mathbf{X}_{n-1} , the columns of \mathbf{X}_n reflect weighted combinations and/or nonlinear transformations of the columns of \mathbf{Y}_n . Many dimensionality reduction algorithms are invertible (or approximately invertible). However, attempting to map a given \mathbf{X}_n back onto the original feature space of \mathbf{X}_0 will usually require $\mathcal{O}(TK^{2n})$ space and therefore becomes intractable as n or K grow large.

Graph measure approaches to computing \mathbf{X}_n

The above dimensionality reduction approaches to approximating a given \mathbf{Y}_n with a lower-dimensional \mathbf{X}_n preserve a (potentially recombined and transformed) mapping back to the original data in \mathbf{X}_0 . We also explore graph measures that instead characterize each feature’s relative *position* in the broader network of interactions and connections. To illustrate the distinction between the two general approaches we explore, suppose a network comprises nodes A ~~and~~B, and C along with several other nodes. If A and B exhibit uncorrelated activity patterns, then by definition the functional connection (correlation) between them will be ~~(by definition)~~ close to 0. However, if A and B each interact with ~~C~~other nodes in similar ways, we might attempt to capture those similarities ~~using a measure that reflects how between A's and B interact with other~~'s interactions with those other members of the network.

In general, graph measures take as input a matrix of interactions (e.g., using the above notation, a K by K correlation matrix or binarized correlation matrix reconstituted from a single timepoint’s row of \mathbf{Y}), and return as output a set of K measures describing how each node (feature) sits within that correlation matrix with respect to the rest of the population. Widely used measures include betweenness centrality (the proportion of shortest paths between each pair of nodes in the population that involves the given node in question; e.g., Barthélemy, 2004; Freeman, 1977; Geisberger et al., 2008; Newman, 2005; Opsahl et al., 2010); diversity and dissimilarity (characterizations of how differently connected a given node is from others in the population; e.g., Lin, 2009; Rao, 1982; Ricotta & Szeidl, 2006); eigenvector centrality and pagerank centrality (measures of how influential a given node is within the broader network; e.g., Bonacich, 2007; Halu et al., 2013; Lohmann et al., 2010; Newman, 2008); transfer entropy and flow coefficients (a measure of how much information is flowing from a given node to other nodes in the network; e.g., Honey et al., 2007; Schreiber, 2000); k -coreness centrality (a measure of the connectivity of a node within its local subgraph; e.g., Alvarez-Hamelin et al., 2005; Christakis & Fowler, 2010); within-module degree (a measure of how many connections a node has to its close neighbors in the network; e.g., Rubinov & Sporns, 2010); participation

374 coefficient (a measure of the diversity of a node's connections to different subgraphs in the network; e.g.,
375 Rubinov & Sporns, 2010); and subgraph centrality (a measure of a node's participation in all of the network's
376 subgraphs; e.g., Estrada & Rodríguez-Velázquez, 2005); among others.

377 For a given graph measure, $\eta : \mathbb{R}^{K \times K} \rightarrow \mathbb{R}^K$, we can use η to transform each row of \mathbf{Y}_n in a way that
378 characterizes the corresponding graph properties of each column. This results in a new T by K matrix,
379 \mathbf{X}_n , that reflects how the features reflected in the columns of \mathbf{X}_{n-1} participate in the network during each
380 timepoint (row).

381 **Dynamic higher-order correlations**

382 Because \mathbf{X}_n has the same shape as the original data \mathbf{X}_0 , approximating \mathbf{Y}_n with a lower-dimensional \mathbf{X}_n enables
383 us to estimate high-order dynamic correlations in a scalable way. Given a T by K input matrix, the output
384 of Equation 4 requires $O(TK^2)$ space to store. Repeated applications of Equation 4 (i.e., computing dynamic
385 correlations between the columns of the outputted dynamic correlation matrix) each require exponentially
386 more space; in general the n^{th} -order dynamic correlations of a T by K timeseries occupies $O(TK^{2n})$ $O(TK^{2^n})$
387 space. However, when we approximate or summarize the output of Equation 4 with a T by K matrix (as
388 described above), it becomes feasible to compute even very high-order correlations in high-dimensional
389 data. Specifically, approximating the n^{th} -order dynamic correlations of a T by K timeseries requires only
390 $O(TK^2)$ additional space— the same as would be required to compute first-order dynamic correlations. In
391 other words, the space required to store $n + 1$ multivariate timeseries reflecting up to n^{th} order correlations
392 in the original data scales linearly with n using our approach (Fig. 8).

393 **Data**

394 We examined two types of data: synthetic data and human functional neuroimaging data. We constructed
395 and leveraged the synthetic data to evaluate our general approach (for a related validation approach see
396 Thompson et al., 2018). Specifically, we tested how well Equation 4 could be used to recover known dynamic
397 correlations using different choices of kernel (κ ; Fig. 9), for each of several synthetic datasets that exhibited
398 different temporal properties. We also simulated higher-order correlations and tested how well Equation 4
399 could recover these correlations using the best kernel from the previous synthetic data analyses. We then
400 applied our approach to a functional neuroimaging dataset to test the hypothesis that ongoing cognitive
401 processing is reflected in high-order dynamic correlations. We used an across-participant classification test
402 to estimate whether dynamic correlations of different orders contain information about which timepoint in
403 a story participants were listening to.

404 **Synthetic data: simulating dynamic first-order correlations**

405 We constructed a total of 40 different multivariate timeseries, collectively reflecting a total of 4 qualitatively
 406 different patterns of dynamic first-order correlations (i.e., 10 datasets reflecting each type of dynamic pat-
 407 tern). Each timeseries comprised 50 features (dimensions) that varied over 300 timepoints. The observations
 408 at each timepoint were drawn from a zero-mean multivariate Gaussian distribution with a covariance matrix
 409 defined for each timepoint as described below. We drew the observations at each timepoint independently
 410 from the draws at all other timepoints; in other words, for each observation $s_t \sim \mathcal{N}(\mathbf{0}, \Sigma_t)$ at timepoint t ,
 411 $p(s_t) = p(s_t | s_{\setminus t})$.

Constant. We generated data with stable underlying correlations to evaluate how Equation 4 characterized correlation “dynamics” when the ground truth correlations were static. We constructed 10 multivariate timeseries whose observations were each drawn from a single (stable) Gaussian distribution. For each dataset (indexed by m), we constructed a random covariance matrix, Σ_m :

$$\underline{\Sigma_m} \equiv \mathbf{C} \mathbf{C}^\top, \text{ where} \quad (11)$$

$$\underline{\mathbf{C}(i, j) \sim \mathcal{N}(0, 1)} \underline{\Sigma_m = \mathbf{C} \mathbf{C}^\top}, \text{ where, and where} \quad (12)$$

412 $i, j \in [1, 2, \dots, 50]$. In other words, all of the observations (for each of the 300 timepoints) within each dataset
 413 were drawn from a multivariate Gaussian distribution with the same covariance matrix, and the 10 datasets
 414 each used a different covariance matrix.

415 **Random.** We generated a second set of 10 synthetic datasets whose observations at each timepoint were
 416 drawn from a Gaussian distribution with a new randomly constructed (using Eqn. 11) covariance matrix.
 417 Because each timepoint’s covariance matrix was drawn independently from the covariance matrices for all
 418 other timepoints, these datasets provided a test of reconstruction accuracy in the absence of any meaningful
 419 underlying temporal structure in the dynamic correlations underlying the data.

Ramping. We generated a third set of 10 synthetic datasets whose underlying correlations changed gradually over time. For each dataset, we constructed two *anchor* covariance matrices using Equation 11, Σ_{start} and Σ_{end} . For each of the 300 timepoints in each dataset, we drew the observations from a multivariate Gaussian distribution whose covariance matrix at each timepoint $t \in [0, \dots, 299]$ was given by

$$\Sigma_t = \left(1 - \frac{t}{299}\right) \Sigma_{\text{start}} + \frac{t}{299} \Sigma_{\text{end}}. \quad (13)$$

420 The gradually changing correlations underlying these datasets allow us to evaluate the recovery of dynamic
421 correlations when each timepoint's correlation matrix is unique (as in the random datasets), but where the
422 correlation dynamics are structured and exhibit first-order autocorrelations (as in the constant datasets).

423 **Event.** We generated a fourth set of 10 synthetic datasets whose underlying correlation matrices exhibited
424 prolonged intervals of stability, interspersed with abrupt changes. For each dataset, we used Equation 11
425 to generate 5 random covariance matrices. We constructed a timeseries where each set of 60 consecutive
426 samples was drawn from a Gaussian with the same covariance matrix. These datasets were intended to
427 simulate a system that undergoes exhibits periods of stability punctuated by occasional abrupt state changes.

428 **Synthetic data: simulating dynamic high-order correlations**

429 We developed an iterative procedure for constructing timeseries data that exhibits known dynamic high-order
430 correlations. The procedure builds on our approach to generating dynamic first-order correlations. Essentially,
431 once we generate a timeseries with known first-order correlations, we can use the known first-order
432 correlations as a template to generate a new timeseries of second-order correlations. In turn, we can
433 generate a timeseries of third-order correlations from the second-order correlations, and so on. In general,
434 we can generate order n correlations given a timeseries of order $n - 1$ correlations, for any $n > 1$. Finally,
435 given the order n timeseries, we can reverse the preceding process to generate an order $n - 1$ timeseries, an
436 order $n - 2$ order timeseries, and so on, until we obtain an order 0 timeseries of simulated data that reflects
437 the chosen high-order dynamics.

The central mathematical operations in our procedure are two functions, $\text{vec}(\cdot)$ and $\text{mat}(\cdot)$. The $\text{vec}(\cdot)$ function takes as input a $K \times K$ symmetric matrix and returns as output a $(\frac{K^2-K}{2} + K)$ -dimensional column vector containing the entries in the upper triangle and diagonal. The $\text{mat}(\cdot)$ function inverts $\text{vec}(\cdot)$ by taking as input a $(\frac{K^2-K}{2} + K)$ -dimensional column vector and returning a $K \times K$ symmetric matrix as output. We can then generate an order n correlation matrix (for one timepoint, t) from an order $n - 1$ template (from the same timepoint) as follows:

$$\Sigma_n(t) = \text{mat}(\text{vec}(\Sigma_{n-1}(t)) \otimes \text{vec}(\Sigma_{n-1}(t))^\top). \quad (14)$$

Given a timeseries of order n correlation matrices, we can draw an order $n - 1$ correlation matrix for each timepoint t using

$$\sigma_{n-1}(t) \sim \mathcal{N}(\mathbf{0}, \Sigma_n(t)) \quad (15)$$

$$\Sigma_{n-1}(t) = \text{mat}(\sigma_{n-1}(t)). \quad (16)$$

438 We can then use repeated applications of Equations 15 and 16 in order to obtain a synthetic dataset.
439 When the template first-order correlations are constructed to exhibit different temporal profiles (e.g.,
440 using the constant, random, ramping, and event procedures described above), the resulting high-order
441 correlations and synthetic data will exhibit the same category of temporal profile.
442 Following our approach to generating synthetic data exhibiting known first-order correlations, we
443 constructed a total of 40 additional multivariate timeseries, collectively reflecting a total of 4 qualitatively
444 different patterns of dynamic correlations (i.e., 10 datasets reflecting each type of dynamic pattern: constant,
445 random, ramping, and event).

446 Functional neuroimaging data collected during story listening

447 We examined an fMRI dataset collected by Simony et al. (2016) that the authors have made publicly available
448 at arks.princeton.edu/ark:/88435/dsp015d86p269k. The dataset comprises neuroimaging data collected as
449 participants listened to an audio recording of a story (intact condition; 36 participants), listened to temporally
450 scrambled recordings of the same story (17 participants in the paragraph-scrambled condition listened to
the paragraphs in a randomized order and 36 in the word-scrambled condition listened to the words in a
451 randomized order), or lay resting with their eyes open in the scanner (rest condition; 36 participants). Full
452 neuroimaging details may be found in the original paper for which the data were collected (Simony et al.,
453 2016).

455 **Hierarchical topographic factor analysis (HTFA).** Following our prior related work, we used HTFA (Manning et al., 2018) to derive a compact representation of the neuroimaging data. In brief, this approach approximates the timeseries of voxel activations (44,415 voxels) using a much smaller number of radial basis function (RBF) nodes (in this case, 700 nodes, as determined by an optimization procedure described by Manning et al., 2018). This provides a convenient representation for examining full-brain network dynamics.
456 All of the analyses we carried out on the neuroimaging dataset were performed in this lower-dimensional
space. In other words, each participant's data matrix, \mathbf{X}_0 , was a number-of-timepoints by 700 matrix of
457 HTFA-derived factor weights (where the row and column labels were matched across participants). Code
458

463 for carrying out HTFA on fMRI data may be found as part of the BrainIAK toolbox (Capota et al., 2017),
464 which may be downloaded at brainiak.org.

465 Temporal decoding

466 We sought to identify neural patterns that reflected participants' ongoing cognitive processing of incoming
467 stimulus information. As reviewed by Simony et al. (2016), one way of homing in on these stimulus-driven
468 neural patterns is to compare activity patterns across individuals (e.g., using ISFC analyses). In particular,
469 neural patterns will be similar across individuals to the extent that the neural patterns under consideration
470 are stimulus-driven, and to the extent that the corresponding cognitive representations are reflected in
471 similar spatial patterns across people (also see Simony & Chang, 2020). Following this logic, we used an
472 across-participant temporal decoding test developed by Manning et al. (2018) to assess the degree to which
473 different neural patterns reflected ongoing stimulus-driven cognitive processing across people –(Fig. 10).
474 The approach entails using a subset of the data to train a classifier to decode stimulus timepoints (i.e.,
475 moments in the story participants listened to) from neural patterns. We use decoding (forward inference)
476 accuracy on held-out data, from held-out participants, as a proxy for the extent to which the inputted neural
477 patterns reflected stimulus-driven cognitive processing in a similar way across individuals.

478 Forward inference and decoding accuracy

479 We used an across-participant correlation-based classifier to decode which stimulus timepoint matched each
480 timepoint's neural pattern –(Fig. 10). We first divided the participants into two groups: a template group,
481 $\mathcal{G}_{\text{template}}$ –(i.e., training data), and a to-be-decoded group, $\mathcal{G}_{\text{decode}}$ –(i.e., test data). We used Equation 7 to
482 compute a DISFC matrix for each group ($\bar{\mathbf{C}}_{\text{template}}$ and $\bar{\mathbf{C}}_{\text{decode}}$, respectively). We then correlated the rows of
483 $\bar{\mathbf{C}}_{\text{template}}$ and $\bar{\mathbf{C}}_{\text{decode}}$ to form a number-of-timepoints by number-of-timepoints decoding matrix, Λ . In this
484 way, the rows of Λ reflected timepoints from the template group, while the columns reflected timepoints
485 from the to-be-decoded group. We used Λ to assign temporal labels to each row $\bar{\mathbf{C}}_{\text{decode}}$ using the row of
486 $\bar{\mathbf{C}}_{\text{template}}$ with which it was most highly correlated. We then repeated this decoding procedure, but using
487 $\mathcal{G}_{\text{decode}}$ as the template group and $\mathcal{G}_{\text{template}}$ as the to-be-decoded group. Given the true timepoint labels (for
488 each group), we defined the *decoding accuracy* as the average proportion of correctly decoded timepoints,
489 across both groups. We defined the *relative decoding accuracy* as the difference between the decoding accuracy
490 and chance accuracy (i.e., $\frac{1}{T}$).

491 **Feature weighting and testing**

492 We sought to examine which types of neural features (i.e., activations, first-order dynamic correlations, and
493 higher-order dynamic correlations) were informative to the temporal decoders. Using the notation above,
494 these features correspond to $\mathbf{X}_0, \mathbf{X}_1, \mathbf{X}_2, \mathbf{X}_3$, and so on.

495 One challenge to fairly evaluating high-order correlations is that if the kernel used in Equation 4 is
496 wider than a single timepoint, each repeated application of the equation will result in further temporal
497 blur. Because our primary assessment metric is temporal decoding accuracy, this unfairly biases against
498 detecting meaningful signal in higher-order correlations (relative to lower-order correlations). We attempted
499 to mitigate temporal blur in estimating each \mathbf{X}_n by using a Dirac δ function kernel (which places all of its
500 mass over a single timepoint; Fig. 9b, [10a](#)) to compute each lower-order correlation ($\mathbf{X}_1, \mathbf{X}_2, \dots, \mathbf{X}_{n-1}$). We
501 then used a new (potentially wider, as described below) kernel to compute \mathbf{X}_n from \mathbf{X}_{n-1} . In this way,
502 temporal blurring was applied only in the last step of computing \mathbf{X}_n . We note that, because each \mathbf{X}_n is a
503 low-dimensional representation of the corresponding \mathbf{Y}_n , the higher-order correlations we estimated reflect
504 true correlations in the data with lower-fidelity than estimates of lower-order correlations. Therefore, even
505 after correcting for temporal blurring, our approach is still biased against finding meaningful signal in
506 higher-order correlations.

507 After computing each $\mathbf{X}_1, \mathbf{X}_2, \dots, \mathbf{X}_{n-1}$ for each participant, we divided participants into two equally sized
508 groups (± 1 for odd numbers of participants): $\mathcal{G}_{\text{train}}$ and $\mathcal{G}_{\text{test}}$. We then further subdivided $\mathcal{G}_{\text{train}}$ into $\mathcal{G}_{\text{train}_1}$
509 and $\mathcal{G}_{\text{train}_2}$. We then computed Λ (temporal correlation) matrices for each type of neural feature, using $\mathcal{G}_{\text{train}_1}$
510 and $\mathcal{G}_{\text{train}_2}$. This resulted in $n + 1$ Λ matrices (one for the original timeseries of neural activations, and one
511 for each of n orders of dynamic correlations). Our objective was to find a set of weights for each of these
512 Λ matrices such that the weighted average of the $n + 1$ matrices yielded the highest decoding accuracy.
513 We used quasi-Newton gradient ascent (Nocedal & Wright, 2006), using decoding accuracy (for $\mathcal{G}_{\text{train}_1}$ and
514 $\mathcal{G}_{\text{train}_2}$) as the objective function to be maximized, to find an optimal set of training data-derived weights,
515 $\phi_{0,1,\dots,n}$, where $\sum_{i=0}^n \phi_i = 1$ and where $\phi_i \geq 0 \forall i \in [0, 1, \dots, n]$.

516 After estimating an optimal set of weights, we computed a new set of $n + 1$ Λ matrices correlating the
517 DISFC patterns from $\mathcal{G}_{\text{train}}$ and $\mathcal{G}_{\text{test}}$ at each timepoint. We use the resulting decoding accuracy of $\mathcal{G}_{\text{test}}$
518 timepoints (using the weights in $\phi_{0,1,\dots,n}$ to average the Λ matrices) to estimate how informative the set of
519 neural features containing up to n^{th} order correlations were.

520 We used a permutation-based procedure to form stable estimates of decoding accuracy for each set of
521 neural features. In particular, we computed the decoding accuracy for each of 10 random group assignments
522 of $\mathcal{G}_{\text{train}}$ and $\mathcal{G}_{\text{test}}$. We report the mean accuracy (along with 95% confidence intervals) for each set of neural

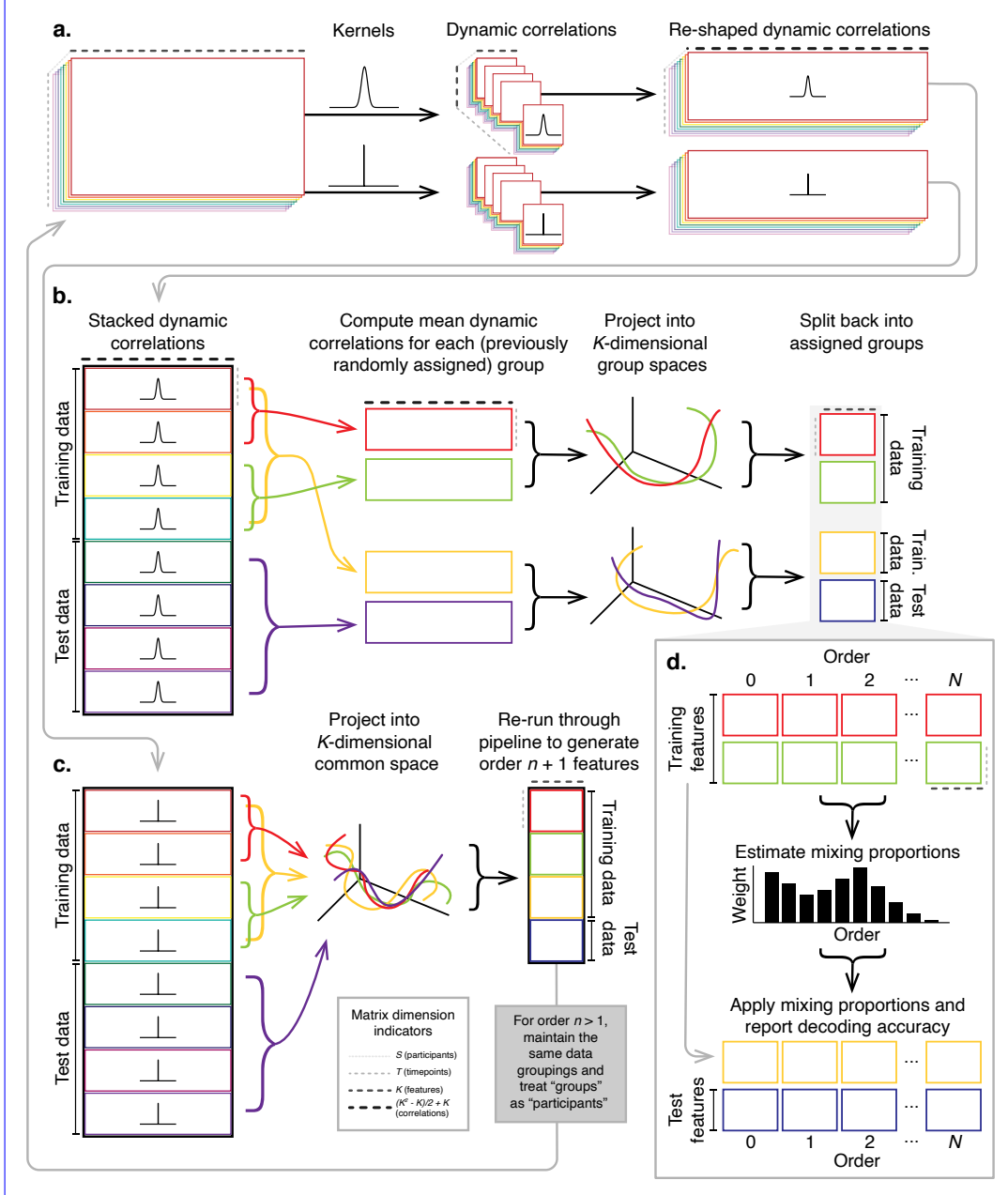


Figure 10: **Decoding analysis pipeline.** **a. Computing dynamic correlations from timeseries data.** Given a timeseries of observations as a $T \times K$ matrix (or a set of S such matrices), we use Equation 4 to compute each participant’s DISFC (relative to other participants in the training or test sub-group, as appropriate). We repeat this process twice—once using the analysis kernel (shown here as a Gaussian in the upper row of the panel), and once using a δ function kernel (lower row of the panel). **b. Projecting dynamic correlations into a lower-dimensional space.** We project the training and test data into K -dimensional spaces to create compact representations of dynamic correlations at the given order (estimated using the analysis kernel). **c. Kernel trick.** We project the dynamic correlations computed using a δ function kernel into a common K -dimensional space. These low-dimensional embeddings are fed back through the analysis pipeline in order to compute features at the next-highest order. **d. Decoding analysis.** We split the training data into two equal groups, and optimize the feature weights (i.e., dynamic correlations at each order) to maximize decoding accuracy. We then apply the trained classifier to the (held-out) test data.

523 features.

524 **Identifying robust decoding results**

525 The temporal decoding procedure we use to estimate which neural features support ongoing cognitive
526 processing is governed by several parameters. In particular, Equation 4 requires defining a kernel function,
527 which can take on different shapes and widths. For a fixed set of neural features, each of these parameters
528 can yield different decoding accuracies. Further, the best decoding accuracy for a given timepoint may be
529 reliably achieved by one set of parameters, whereas the best decoding accuracy for another timepoint might
530 be reliably achieved by a different set of parameters, and the best decoding accuracy across *all* timepoints
531 might be reliably achieved by still another different set of parameters. Rather than attempting to maximize
532 decoding accuracy, we sought to discover the trends in the data that were robust to classifier parameters
533 choices. Specifically, we sought to characterize how decoding accuracy varied (under different experimental
534 conditions) as a function of which neural features were considered.

535 To identify decoding results that were robust to specific classifier parameter choices, we repeated our
536 decoding analyses after substituting into Equation 4 each of a variety of kernel shapes and widths. We
537 examined Gaussian (Fig. 9c), Laplace (Fig. 9d), and Mexican Hat (Fig. 9e) kernels, each with widths of 5, 10,
538 20, and 50 samples. We then report the average decoding accuracies across all of these parameter choices.
539 This enabled us to (partially) factor out performance characteristics that were parameter-dependent, within
540 the set of parameters we examined.

541 **Reverse inference**

542 The dynamic patterns we examined comprise high-dimensional correlation patterns at each timepoint. To
543 help interpret the resulting patterns in the context of other studies, we created summary maps by computing
544 the across-timepoint average pairwise correlations at each order of analysis (first order, second order, etc.).
545 We selected the 10 strongest (absolute value) correlations at each order. Each correlation is between the
546 dynamic activity patterns (or patterns of dynamic high-order correlations) measured at two RBF nodes
547 (see *Hierarchical Topographic Factor Analysis*). Therefore, the 10 strongest correlations involved up to 20 RBF
548 nodes. Each RBF defines a spatial function whose activations range from 0 to 1. We constructed a map
549 of RBF components that denoted the endpoints of the 10 strongest correlations (we set each RBF to have a
550 maximum value of 1). We then carried out a meta analysis using Neurosynth (Rubin et al., 2017) to identify
551 the 10 terms most commonly associated with the given map. This resulted in a set of 10 terms associated
552 with the average dynamic correlation patterns at each order.

553 **Acknowledgements**

554 We acknowledge discussions with Luke Chang, Vassiki Chauhan, Hany Farid, Paxton Fitzpatrick, Andrew
555 Heusser, Eshin Jolly, Aaron Lee, Qiang Liu, Matthijs van der Meer, Judith Mildner, Gina Notaro, Stephen
556 Satterthwaite, Emily Whitaker, Weizhen Xie, and Kirsten Ziman. Our work was supported in part by NSF
557 EPSCoR Award Number 1632738 to J.R.M. and by a sub-award of DARPA RAM Cooperative Agreement
558 N66001-14-2-4-032 to J.R.M. The content is solely the responsibility of the authors and does not necessarily
559 represent the official views of our supporting organizations.

560 **Author contributions**

561 Concept: J.R.M. Implementation: T.H.C., L.L.W.O., and J.R.M. Analyses: L.L.W.O. and J.R.M. Writing:
562 L.L.W.O. and J.R.M.

563 **References**

- 564 Allen, E. A., Damaraju, E., Plis, S. M., Erhardt, E. B., Eichele, T., & Calhoun, V. D. (2012). Tracking
565 whole-brain connectivity dynamics in the resting state. *Cerebral Cortex*, 24(3), 663–676.
- 566 Alvarez-Hamelin, I., Dall'Asta, L., Barrat, A., & Vespignani, A. (2005). *k*-corr decomposition: a tool for the
567 visualization of large scale networks. *arXiv*, cs/0504107v2.
- 568 Baldassano, C., Chen, J., Zadbood, A., Pillow, J. W., Hasson, U., & Norman, K. A. (2017). Discovering event
569 structure in continuous narrative perception and memory. *Neuron*, 95(3), 709–721.
- 570 Barthélémy, M. (2004). Betweenness centrality in large complex networks. *European Physical Journal B*, 38,
571 163–168.
- 572 Bassett, D., Meyer-Lindenberg, A., Achard, S., Duke, T., & Bullmore, E. (2006, December). Adaptive
573 reconfiguration of fractal small-world human brain functional networks. *Proceedings of the National
574 Academy of Sciences, USA*, 103(51), 19518–23.
- 575 Beaty, R. E., Benedek, M., Silvia, P. J., & Schacter, D. L. (2016). Creative cognition and brain network
576 dynamics. *Trends in Cognitive Sciences*, 20(2), 87–95.
- 577 Betzel, R. F., Byrge, L., Esfahlani, F. Z., & Kennedy, D. P. (2019). Temporal fluctuations in the brain's modular
578 architecture during movie-watching. *bioRxiv*, doi.org/10.1101/750919.

- 579 Bonacich, P. (2007). Some unique properties of eigenvector centrality. *Social Networks*, 29(4), 555–564.
- 580 Bullmore, E., & Sporns, O. (2009). Complex brain networks: graph theoretical analysis of structural and
581 functional systems. *Nature Reviews Neuroscience*, 10(3), 186–198.
- 582 Capota, M., Turek, J., Chen, P.-H., Zhu, X., Manning, J. R., Sundaram, N., ... Shin, Y. S. (2017). *Brain imaging
583 analysis kit*. Retrieved from <https://doi.org/10.5281/zenodo.59780>
- 584 Chang, C., & Glover, G. H. (2010). Time-frequency dynamics of resting-state brain connectivity measured
585 with fMRI. *NeuroImage*, 50, 81–98.
- 586 Chien, H.-Y. S., & Honey, C. J. (2019). Constructing and forgetting temporal context in the human cerebral
587 cortex. *bioRxiv*, doi.org/10.1101/761593.
- 588 Christakis, N. A., & Fowler, J. H. (2010). Social network sensors for early detection of contagious outbreaks.
589 *PLoS One*, 5(9), e12948.
- 590 Combrisson, E., Vallat, R., O'Reilly, C., Jas, M., Pascarella, A., l Saive, A., ... Jerbi, K. (2019). Visbrain: a
591 multi-purpose GPU-accelerated open-source suite for multimodal brain data visualization. *Frontiers in
592 Neuroinformatics*, 13(14), 1–14.
- 593 Comon, P., Jutten, C., & Herault, J. (1991). Blind separation of sources, part II: Problems statement. *Signal
594 Processing*, 24(1), 11 - 20.
- 595 Demertzi, A., Tagliazucchi, E., Dehaene, S., Deco, G., Barttfeld, P., Raimondo, F., ... Sitt, J. D. (2019). Human
596 consciousness is supported by dynamic complex patterns of brain signal coordination. *Science Advances*,
597 5(2), eaat7603.
- 598 Estrada, E., & Rodríguez-Velázquez, J. A. (2005). Subgraph centrality in complex networks. *Physical Review
599 E*, 71(5), 056103.
- 600 Etzel, J. A., Gazzola, V., & Keysers, C. (2009). An introduction to anatomical ROI-based fMRI classification.
601 *Brain Research*, 1281, 114–125.
- 602 Fallon, J., Ward, P., Parkes, L., Oldham, S., Arnatkevičiūtė, A., Fornito, A., & Fulcher, B. D. (2019).
603 Timescales of spontaneous activity fluctuations relate to structural connectivity in the brain. *bioRxiv*,
604 doi.org/10.1101/655050.
- 605 Fong, A. H. C., Yoo, K., Rosenberg, M. D., Zhang, S., Li, C.-S. R., Scheinost, D., ... Chun, M. M. (2019).
606 Dynamic functional connectivity during task performance and rest predicts individual differences in
607 attention across studies. *NeuroImage*, 188, 14–25.

- 608 Freeman, L. C. (1977). A set of measures of centrality based on betweenness. *Sociometry*, 40(1), 35–41.
- 609 Friston, K. (2000). The labile brain. i. neuronal transients and nonlinear coupling. *Phil. Trans. Roy. Soc. Lon.*,
610 355B, 215–236.
- 611 Geisberger, R., Sanders, P., & Schultes, D. (2008). Better approximation of betweenness centrality. *Proceedings
612 of the meeting on Algorithm Engineering and Experiments*, 90–100.
- 613 Gershman, S., Blei, D., Pereira, F., & Norman, K. (2011). A topographic latent source model for fMRI data.
614 *NeuroImage*, 57, 89–100.
- 615 Gonzalez-Castillo, J., Caballero-Gaudes, C., Topolski, N., Handwerker, D. A., Pereira, F., & Bandettini, P. A.
616 (2019). Imaging the spontaneous flow of thought: distinct periods of cognition contribute to dynamic
617 functional connectivity during rest. *NeuroImage*, 202(116129).
- 618 Grossberg, S. (1988). Nonlinear neural networks: Principles, mechanisms, and architectures. *Neural
619 networks*, 1(1), 17–61.
- 620 Halu, A., Mondragón, R. J., Panzarasa, P., & Bianconi, G. (2013). Multiplex PageRank. *PLoS One*, 8(10),
621 e78293.
- 622 Hasson, U., Chen, J., & Honey, C. J. (2015). Hierarchical process memory: memory as an integral component
623 of information processing. *Trends in Cognitive Science*, 19(6), 304–315.
- 624 Hasson, U., Yang, E., Vallines, I., Heeger, D. J., & Rubin, N. (2008). A hierarchy of temporal receptive windows
625 in human cortex. *Journal of Neuroscience*, 28(10), 2539–2550. doi: 10.1523/JNEUROSCI.5487-07.2008
- 626 Haxby, J. V., Gobbini, M. I., Furey, M. L., Ishai, A., Schouten, J. L., & Pietrini, P. (2001). Distributed and
627 overlapping representations of faces and objects in ventral temporal cortex. *Science*, 293, 2425–2430.
- 628 Hinton, G. E., & Salakhutdinov, R. R. (2006). Reducing the dimensionality of data with neural networks.
629 *Science*, 313(5786), 504–507.
- 630 Honey, C. J., Kötter, R., Breakspear, M., & Sporns, O. (2007). Network structure of cerebral cortex shapes
631 functional connectivity on multiple time scales. *Proceedings of the National Academy of Science USA*, 104(24),
632 10240–10245.
- 633 Honey, C. J., Thesen, T., Donner, T. H., Silbert, L. J., Carlson, C. E., Devinsky, O., . . . Hasson, U. (2012). Slow
634 cortical dynamics and the accumulation of information over long timescales. *Neuron*, 76, 423–434. doi:
635 10.1016/j.neuron.2012.08.011

- 636 Huth, A. G., de Heer, W. A., Griffiths, T. L., Theunissen, F. E., & Gallant, J. L. (2016). Natural speech reveals
637 the semantic maps that tile human cerebral cortex. *Nature*, 532, 453–458.
- 638 Huth, A. G., Nisimoto, S., Vu, A. T., & Gallant, J. L. (2012). A continuous semantic space describes
639 the representation of thousands of object and action categories across the human brain. *Neuron*, 76(6),
640 1210-1224.
- 641 Jutten, C., & Herault, J. (1991). Blind separation of sources, part I: An adaptive algorithm based on
642 neuromimetic architecture. *Signal Processing*, 24(1), 1–10.
- 643 Kamitani, Y., & Tong, F. (2005). Decoding the visual and subjective contents of the human brain. *Nature*
644 *Neuroscience*, 8, 679–685.
- 645 Landau, E. (1895). Zur relativen Wertbemessung der Turnierresultate. *Deutsches Wochenschach*, 11, 366–369.
- 646 Lee, C. S., Aly, M., & Baldassano, C. (2020). Anticipation of temporally structured events in the brain.
647 *bioRxiv*, 10.1101/2020.10.14.338145.
- 648 Lee, D. D., & Seung, H. S. (1999). Learning the parts of objects by non-negative matrix factorization. *Nature*,
649 401, 788–791.
- 650 Lerner, Y., Honey, C. J., Katkov, M., & Hasson, U. (2014). Temporal scaling of neural responses to compressed
651 and dilated natural speech. *Journal of Neurophysiology*, 111, 2433–2444.
- 652 Lerner, Y., Honey, C. J., Silbert, L. J., & Hasson, U. (2011). Topographic mapping of a hierarchy of
653 temporal receptive windows using a narrated story. *Journal of Neuroscience*, 31(8), 2906-2915. doi: 10.1523/
654 JNEUROSCI.3684-10.2011
- 655 Liégeois, R., Li, J., Kong, R., Orban, C., De Ville, D. V., Ge, T., … Yeo, B. T. T. (2019). Resting brain
656 dynamics at different timescales capture distinct aspects of human behavior. *Nature Communications*,
657 10(2317), doi.org/10.1038/s41467-019-10317-7.
- 658 Lin, J. (2009). Divergence measures based on the Shannon entropy. *IEEE Transactions on Information Theory*,
659 37(1), 145–151.
- 660 Lohmann, G., Margulies, D. S., Horstmann, A., Pleger, B., Lepsius, J., Goldhahn, D., … Turner, R. (2010).
661 Eigenvector centrality mapping for analyzing connectivity patterns in fMRI data of the human brain.
662 *PLoS One*, 5(4), e10232.
- 663 Lurie, D., Kessler, D., Bassett, D., Betzel, R., Breakspear, M., Keilholz, S., … Calhoun, V. (2018). On the
664 nature of time-varying functional connectivity in resting fMRI. *PsyArXiv*, doi.org/10.31234/osf.io/xtzre.

- 665 Mack, M. L., Preston, A. R., & Love, B. C. (2017). Medial prefrontal cortex compresses concept representations
666 through learning. *bioRxiv*, doi.org/10.1101/178145.
- 667 Mairal, J., Ponce, J., Sapiro, G., Zisserman, A., & Bach, F. R. (2009). Supervised dictionary learning. *Advances*
668 *in Neural Information Processing Systems*, 1033–1040.
- 669 Mairal, J. B., Bach, F., Ponce, J., & Sapiro, G. (2009). Online dictionary learning for sparse coding. *Proceedings*
670 *of the 26th annual international conference on machine learning*, 689–696.
- 671 Manning, J. R., Ranganath, R., Norman, K. A., & Blei, D. M. (2014). Topographic factor analysis: a Bayesian
672 model for inferring brain networks from neural data. *PLoS One*, 9(5), e94914.
- 673 Manning, J. R., Zhu, X., Willke, T. L., Ranganath, R., Stachenfeld, K., Hasson, U., . . . Norman, K. A. (2018).
674 A probabilistic approach to discovering dynamic full-brain functional connectivity patterns. *NeuroImage*,
675 180, 243–252.
- 676 McInnes, L., Healy, J., & Melville, J. (2018). UMAP: Uniform manifold approximation and projection for
677 dimension reduction. *arXiv*, 1802(03426).
- 678 McIntosh, A. R., & Jirsa, V. K. (2019). The hidden repertoire of brain dynamics and dysfunction. *Network*
679 *Neuroscience*, doi.org/10.1162/netn_a_00107.
- 680 Mitchell, T., Shinkareva, S., Carlson, A., Chang, K., Malave, V., Mason, R., & Just, M. (2008). Predicting
681 human brain activity associated with the meanings of nouns. *Science*, 320(5880), 1191.
- 682 Newman, M. E. J. (2005). A measure of betweenness centrality based on random walks. *Social Networks*, 27,
683 39–54.
- 684 Newman, M. E. J. (2008). The mathematics of networks. *The New Palgrave Encyclopedia of Economics*, 2, 1–12.
- 685 Nishimoto, S., Vu, A., Naselaris, T., Benjamini, Y., Yu, B., & Gallant, J. (2011). Reconstructing visual
686 experience from brain activity evoked by natural movies. *Current Biology*, 21, 1 - 6.
- 687 Nocedal, J., & Wright, S. J. (2006). *Numerical optimization*. New York: Springer.
- 688 Norman, K. A., Newman, E., Detre, G., & Polyn, S. M. (2006). How inhibitory oscillations can train neural
689 networks and punish competitors. *Neural Computation*, 18, 1577–1610.
- 690 Opsahl, T., Agneessens, F., & Skvoretz, J. (2010). Node centrality in weighted networks: generalizing degree
691 and shortest paths. *Social Networks*, 32, 245–251.

- 692 Park, H.-J., Friston, K. J., Pae, C., Park, B., & Razi, A. (2018). Dynamic effective connectivity in resting state
693 fMRI. *NeuroImage*, 180, 594–608.
- 694 Pearson, K. (1901). On lines and planes of closest fit to systems of points in space. *The London, Edinburgh,
695 and Dublin Philosophical Magazine and Journal of Science*, 2, 559–572.
- 696 Pereira, F., Lou, B., Pritchett, B., Ritter, S., Gershman, S. J., Kanwisher, N., ... Fedorenko, E. (2018). Toward
697 a universal decoder of linguistic meaning from brain activation. *Nature Communications*, 9(963), 1–13.
- 698 Preti, M. G., Bolton, T. A. W., & Van De Ville, D. (2017). The dynamic functional connectome: state-of-the-art
699 and perspectives. *NeuroImage*, 160, 41–54.
- 700 Rao, C. R. (1982). Diversity and dissimilarity coefficients: a unified approach. *Theoretical Population Biology*,
701 21(1), 24–43.
- 702 Reimann, M. W., Nolte, M., Scolamiero, M., Turner, K., Perin, R., Chindemi, G., ... Markram, H. (2017).
703 Cliques of neurons bound into cavities provide a missing link between structure and function. *Frontiers
704 in Computational Neuroscience*, 11(48), 1–16.
- 705 Ricotta, C., & Szeidl, L. (2006). Towards a unifying approach to diversity measures: Bridging the gap
706 between the Shannon entropy and Rao's quadratic index. *Theoretical Population Biology*, 70(3), 237–243.
- 707 Roy, D. S., Park, Y.-G., Ogawa, S. K., Cho, J. H., Choi, H., Kamensky, L., ... Tonegawa, S. (2019). Brain-
708 wide mapping of contextual fear memory engram ensembles supports the dispersed engram complex
709 hypothesis. *bioRxiv*, doi.org/10.1101/668483.
- 710 Rubin, T. N., Kyoejo, O., Gorgolewski, K. J., Jones, M. N., Poldrack, R. A., & Yarkoni, T. (2017). Decoding
711 brain activity using a large-scale probabilistic functional-anatomical atlas of human cognition. *PLoS
712 Computational Biology*, 13(10), e1005649.
- 713 Rubinov, M., & Sporns, O. (2010). Complex network measures of brain connectivity: uses and interpreta-
714 tions. *NeuroImage*, 52, 1059–1069.
- 715 Schreiber, T. (2000). Measuring information transfer. *Physical Review Letters*, 85(2), 461–464.
- 716 Shappell, H., Caffo, B. S., Pekar, J. J., & Lindquist, M. A. (2019). Improved state change estimation in
717 dynamic functional connectivity using hidden semi-Markov models. *NeuroImage*, 191, 243–257.
- 718 Simony, E., & Chang, C. (2020). Analysis of stimulus-induced brain dynamics during naturalistic paradigms.
719 *NeuroImage*, 216, 116461.

- 720 Simony, E., Honey, C. J., Chen, J., & Hasson, U. (2016). Dynamic reconfiguration of the default mode
721 network during narrative comprehension. *Nature Communications*, 7(12141), 1–13.
- 722 Sizemore, A. E., Giusti, C., Kahn, A., Vettel, J. M., Betzel, R. F., & Bassett, D. S. (2018). Cliques and cavities
723 in the human connectome. *Journal of Computational Neuroscience*, 44(1), 115–145.
- 724 Solomon, S. H., Medaglia, J. D., & Thompson-Schill, S. L. (2019). Implementing a concept network model.
725 *Behavior Research Methods*, 51, 1717–1736.
- 726 Spearman, C. (1904). General intelligence, objectively determined and measured. *American Journal of
727 Psychology*, 15, 201–292.
- 728 Sporns, O., & Honey, C. J. (2006). Small worlds inside big brains. *Proceedings of the National Academy of
729 Science USA*, 103(51), 19219–19220.
- 730 Thompson, W. H., Richter, C. G., Plavén-Sigray, P., & Fransson, P. (2018). Simulations to benchmark
731 time-varying connectivity methods for fMRI. *PLoS Computational Biology*, 14(5), e1006196.
- 732 Tipping, M. E., & Bishop, C. M. (1999). Probabilistic principal component analysis. *Journal of Royal Statistical
733 Society, Series B*, 61(3), 611–622.
- 734 Toker, D., & Sommer, F. T. (2019). Information integration in large brain networks. *PLoS Computational
735 Biology*, 15(2), e1006807.
- 736 Tong, F., & Pratte, M. S. (2012). Decoding patterns of human brain activity. *Annual Review of Psychology*, 63,
737 483–509.
- 738 Turk-Browne, N. B. (2013). Functional interactions as big data in the human brain. *Science*, 342, 580–584.
- 739 van der Maaten, L. J. P., & Hinton, G. E. (2008). Visualizing high-dimensional data using t-SNE. *Journal of
740 Machine Learning Research*, 9, 2579–2605.
- 741 Vidaurre, D., Abeysuriya, R., Becker, R., Quinn, A. J., Alfaro-Almagro, F., Smith, S. M., & Woolrich, M. W.
742 (2018). Discovering dynamic brain networks from big data in rest and task. *NeuroImage*, 180, 646–656.
- 743 Zar, J. H. (2010). *Biostatistical analysis*. Prentice-Hall/Pearson.
- 744 Zheng, M., Allard, A., Hagmann, P., & Serrano, M. A. (2019). Geometric renormalization unravels self-
745 similarity of the multiscale human connectome. *arXiv*, 1904.11793.
- 746 Zou, Y., Donner, R. V., Marwan, N., Donges, J. F., & Kurths, J. (2019). Complex network approaches to
747 nonlinear time series analysis. *Physics Reports*, 787, 1–97.